© 2019. Published by The Company of Biologists Ltd | Journal of Experimental Biology (2019) 222, jeb201459. doi:10.1242/jeb.201459

RESEARCH ARTICLE

The roles of joint tissues and jaw muscles in palatal biomechanics of the savannah monitor (*Varanus exanthematicus*) and their significance for cranial kinesis

Alec T. Wilken*, Kevin M. Middleton, Kaleb C. Sellers, Ian N. Cost and Casey M. Holliday

ABSTRACT

Numerous vertebrates exhibit cranial kinesis, or movement between bones of the skull and mandible other than at the jaw joint. Many kinetic species possess a particular suite of features to accomplish this movement, including flexible cranial joints and protractor musculature. Whereas the musculoskeletal anatomy of these kinetic systems is well understood, how these joints are biomechanically loaded, how different soft tissues affect joint loading and kinetic capacity, and how the protractor musculature loads the skull remain poorly understood. Here, we present a finite element model of the savannah monitor, *Varanus exanthematicus*, a modestly kinetic lizard, to better elucidate the roles of soft tissue in mobile joints and protractor musculature in cranial loading. We describe the 3D resultants of jaw muscles and the histology of palatobasal, otic and jaw joints. We tested the effects of joint tissue type, bite point and muscle load to evaluate the biomechanical role of muscles on the palate and braincase. We found that the jaw muscles have significant mediolateral components that can impart stability across palatocranial joints. Articular tissues affect the magnitude of strains experienced around the palatobasal and otic joints. Without protractor muscle loading, the palate, quadrate and braincase experience higher strains, suggesting this muscle helps insulate the braincase and palatoquadrate from high loads. We found that the cross-sectional properties of the bones of *V. exanthematicus* are well suited for performing under torsional loads. These findings suggest that torsional loading regimes may have played a more important role in the evolution of cranial kinesis in lepidosaurs than previously appreciated.

KEY WORDS: Muscle loading, Cartilage, Evolution, Reptile, Skull

INTRODUCTION

The vertebrate skull is a complicated organ that must protect the brain and sensory capsules while also transmitting feeding-generated forces away from these sensory organs. Although several vertebrate lineages have sutured their skulls into one rigid unit, such as mammals and crocodyliforms, many others instead retain flexible skulls in the form of cranial kinesis. Lepidosauria (tuataras, lizards and snakes) is an ideal superorder for testing form and function relationships in the context of cranial kinesis because of the diverse feeding behaviors, skull shapes and kinetic competency (Metzger, 2002). The skull of lepidosaurs has a complex mix of functional trade-offs and constraints (Schwenk, 2000) and it has been argued that cranial kinesis is a result of these constraints and trade-offs (Herrel et al., 2000; Evans, 2003).

Cranial kinesis is accomplished through a suite of features including flexible palatocranial and craniofacial joints, flexure zones within bones, and protractor and jaw musculature (Bout and Zweers, 2001; Metzger, 2002; Holliday and Witmer, 2008). Squamates and birds, the two tetrapod groups whose extant members exhibit kinesis, demonstrate several different types of cranial kinesis based on which joints are mobile and their orientations of excursion (Bout and Zweers, 2001; Metzger, 2002; Montuelle and Williams, 2015). These movements are presumably mediated by activities of the protractor musculature, which link the palate to the braincase; however, little is known about how these muscles function and load the skull during feeding. Protractor muscles help propel the palate in studied examples of avian prokinesis (pigeons; Bermejo et al., 1992), but their activity and functional significance remain unclear in most lizard species. Although Herrel et al. (2007) found that large protractor muscles in geckos aid in bite speed via actively propelling kinetic linkages, the majority of lizard species do not show significant kinesis yet still possess protractor muscles. This suggests the muscles may not promote movements of the palatal and facial units of the skull in akinetic animals but instead may serve as postural muscles that actively resist movements within the skull and may insulate the braincase and cranial joints from feeding-generated forces (Holliday and Witmer, 2008; Moazen et al., 2009). To investigate how protractor muscles might load the palate and braincase of lizards during feeding, we used finite element modeling to explore the biomechanical performance of the cranium of a purportedly modestly kinetic lizard species, the savannah monitor (*Varanus exanthematicus*; Smith and Hylander, 1985).

Species of the lizard genus *Varanus* have been central to understanding the mechanical underpinnings of cranial kinesis. Frazzetta (1962) and Rieppel (1978) proposed that varanids and many other lizard groups display a quadric-crank mechanism in which movements about the otic joint of the quadrate (streptostyly), palatobasal joint and craniofacial hinge (mesokinesis) resulted in the elevation of the facial skeleton relative to the braincase. Smith and Hylander (1985) found that dorsoventral movement occurs about the mesokinetic frontoparietal joint of *V. exanthematicus*, although Metzger (2002) warned that the reported magnitude of this movement may have fallen within the range of error of the strain transducers.

The *Varanus* cranium is a broad, mediolateral and highly fenestrated braced frame (McCurry et al., 2015) and supports its braincase with various skeletal elements such as the epipterygoids (Metzger, 2002), muscular elements such as the protractor musculature (Holliday and Witmer, 2008; Moazen et al., 2009), and a complex network of cranial joints (Holliday and Witmer, 2008).

Department of Pathology and Anatomical Sciences, University of Missouri, M263, Medical Sciences Building, Columbia, MO 65212, USA.

*Author for correspondence (atwxb6@mail.missouri.edu)

A.T.W., 0000-0003-3943-938X; K.M.M., 0000-0003-4704-1064; K.C.S., 0000-0002-3588-9562; I.N.C., 0000-0002-5087-6823; C.M.H., 0000-0001-8210-8434

Received 9 February 2019; Accepted 23 August 2019

Other important cranial features of the *Varanus* cranium include its robust pterygoid and quadrate bones (Fig. 1), which ossify relatively early in development, indicating load-bearing capacity (Werneburg et al., 2015). Although the skeletal anatomy of kinetically competent lepidosaurs like *Varanus* is relatively well known, we understand little about the roles of different joint articular tissues, loading by the protractor musculature and the loading environments of the palate and how these factors affect the feeding system.

Species of lizards use a mixture of joint types to facilitate movement including sutures (mesokinetic joint), diarthroses (palatobasal and jaw joints), synchondroses (otic joints) and, in the lower jaws, syndesmoses (mandibular symphyses; Holliday et al., 2010). These joints likely result from developmental processes at the interfaces of endochondral and membranous elements of the skull (Payne et al., 2011) while mediating biomechanical functions (Mezzasalma et al., 2014). Previous studies have shown the capacity for streptostylic movement reduces joint reaction forces between the quadrate and pterygoid (Moazen et al., 2009). Other biomechanical studies of non-mobile articular tissue in the lepidosaur skull have shown that sutures redistribute strain throughout the skull (Curtis et al., 2013). Similarly, a synovial articulation between the epipterygoid and pterygoid likely decreases the joint reaction forces between them (Moazen et al., 2009).

Linking the medial surface of the palate to the lateral surface of the braincase, the protractor musculature (m. protractor pterygoideus, mPPt; m. levator pterygoideus, mLPt) is thought to either power cranial kinesis or protect the braincase and growth zones from the forces of feeding (Holliday and Witmer, 2008). Electromyographic studies of geckoes show mPPt is active during elevation of the rostrum about the mesokinetic joint during the opening phase of the gape cycle and in display (Herrel et al., 1999), although muscle activation is not necessary for snout protraction and elevation to occur (Herrel et al., 2000). Similarly, m. protractor quadratus et pterygoideus is active during beak elevation about the prokinetic, craniofacial hinge of some birds (Bout and Zweers, 2001; Bermejo et al., 1992). However, comparable EMG data are still lacking for most other species of lizards, including those that possess protractor muscles yet are considered akinetic (Metzger, 2002; Evans, 2003; Herrel et al., 2007). Additionally, because tensile and shear stresses may have adverse effects on the epiphyses that form parts of the palatobasal and otic joints (Carter and Beaupré, 2001), muscle contractions may be an effective means of reorienting and dampening these forces and thus reducing the likelihood of bone failure (Curry, 2002). Thus, besides actuating snout elevation or other movements, protractor muscles may also stiffen the palatocranial junction using eccentric contractions and thus mediate forces transmitted through the cranium.

We employed computational modeling approaches including finite element modeling (FEA) to explore the how intracranial joints in *V. exanthematicus* are biomechanically loaded. Biological applications of FEA, an engineering approach used to evaluate how structures perform under different loads and constraints, have grown in recent years (e.g. Rayfield, 2007; Parr et al., 2012; Sellers et al., 2017; Cost et al., 2019). FEA has been used to explore hypotheses of cranial form and function (e.g. Soons et al., 2010; Santana and Dumont, 2011; McCurry et al., 2015), and the effects of soft tissue on non-mobile cranial joints (e.g. Curtis et al., 2013; Jones et al., 2017), and to create artificial morphologies (e.g. Moazen et al., 2009) and joint tissues to test different loading conditions. Although FEA is not a substitute for *in vivo* experimentation, it is a powerful tool to learn how a morphological structure is loaded under a given set of assumptions. Here, we utilized FEA to explore the effects of different soft tissue materials in flexible intracranial joints and the role of the mPPt musculature in palatal biomechanics in *V. exanthematicus* by modulating soft tissue material properties in flexible joints and selectively activating jaw muscles. We addressed the following questions. Do different articular tissues in flexible joints generate different loading patterns? How do mPPt, mLPt and m. pterygoideus (mPt) work to load the palate and intracranial joints? Do the loading patterns generated by the protractor musculature show evidence of insulating chondral (i.e. cartilage-capped) joints that have sensitive epiphyses? If inactivation of protractor muscles shows greater strain, especially tensile strain, on chondral joints than when all muscles are maximally active, this would support the hypothesis of protractor muscles functioning as strain insulators in akinetic lizards. New findings such as these will inform later experimental and evolutionary studies of cranial function not only in lizards but also in other vertebrates.

MATERIALS AND METHODS

Specimen information and model construction

Two individuals of *Varanus exanthematicus* (Bosc 1792) [Ohio University Vertebrate Collections (OUVC) 10414 and 10417] were acquired following euthanasia and immersed in 70% ethanol because of previous injections of bone-labeling dyes so as leach out the dyes from the specimen (McElroy et al., 2008; Holliday et al., 2010; Williams and Holliday, Ohio University: OH IACUC U06-09). Individual OUVC 10414 was micro-computed tomography (microCT) scanned (GE eXplore locus, 45 µm; Ohio University), used to model the skull (Figs 1 and 2A), dissected for jaw muscle architecture (Tables S1 and S2) and processed for histology (Holliday et al., 2010; Payne et al., 2011) (Fig. 3H–J). Individual OUVC 10417 was immersed in 3–7% I_2KI for diffusible iodine-based contrast-enhanced computed tomography (diceCT) (Holliday et al., 2013; Gignac et al., 2016) for 6 weeks and CT scanned (Zeiss Xradia Versa 410, 44 µm slice thickness; University of Missouri) (Fig. 3B–G).

Histology

Histological sections of symphyseal, otic, palatobasal, jaw and frontoparietal joints were collected from OUVC 10414 after microCT scanning. Methods and findings from the mandibular symphysis were presented in Holliday et al. (2010). Briefly, the specimen was embedded in methyl methacrylate (MMA) and dibutyl phthalate (DBP) and sectioned using a motorized rotary microtome (Leica Microsystems) at 5 µm thickness and alternatingly stained for connective tissues. The remaining joints were processed following methods outlined in Payne et al. (2011) for thick sections. Briefly, specimens were embedded in MMA and DBP, cut and polished using the EXAKT cutting and Grinding System (EXAKT Technologists, Oklahoma City, OK, USA), ground and polished to a final thickness of 25–35 µm and left unstained or stained with Sanderson's Rapid Bone Stain and Van Gieson's Picrofuschsin. Slides were scanned using an Epson V800 Scanner or Aperio CS2 slide scanner (Fig. 3H–J).

Model construction

CT data were viewed and segmented in Avizo v5.2 and v9 (Thermo Fisher Scientific, Waltham, MA, USA) to produce a 3D model of *V. exanthematicus* cranial skeletal anatomy (Figs 1 and 2A). This model was then imported into Geomagic Studio v7 and v13 (3D Systems, Rock Hill, SC, USA) where the model was cleaned and aligned to proper axes, with z being rostral–caudal, y being dorsal–ventral, x being medial–lateral, and the point (0,0,0) being in line with the jaw joint ventral to the occipital process. The model was then imported into Strand7 (Beaufort Analysis, Sydney, NSW, Australia) where it was meshed for modeling as four-noded tetrahedra (Fig. 2D).

Journal of Experimental Biology (2019) 222, jeb201459. doi:10.1242/jeb.201459

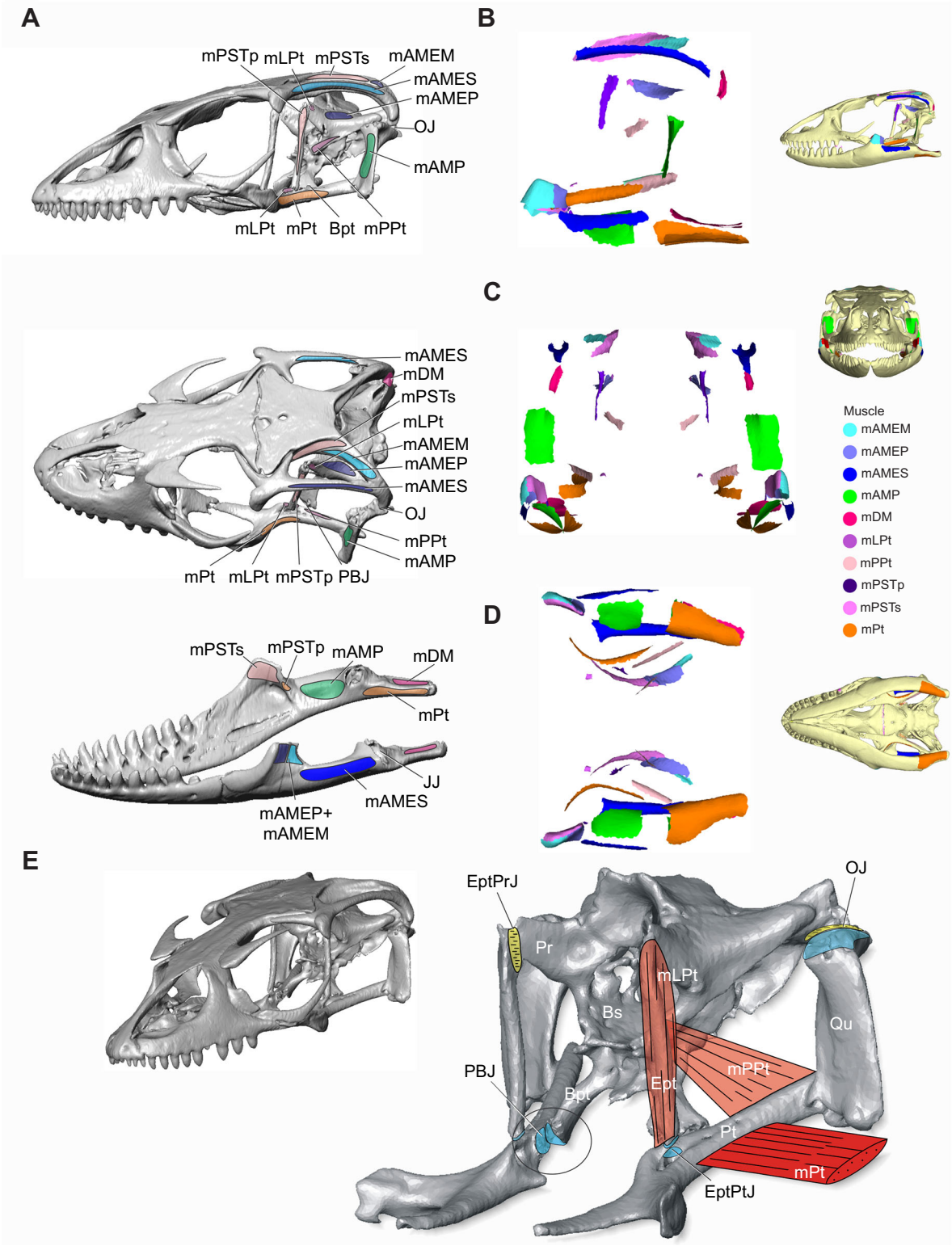

Fig. 1. General cranial anatomy and jaw muscle anatomy of *Varanus exanthematicus* showing maps of muscle attachments, joints and bones associated with palatocranial biomechanics. (A) Detailed image of skull and jaw muscle attachments of *V. exanthematicus*, in left lateral and left oblique dorsal views of the cranium and mandible (modified from Holliday, 2009). (B–D) Muscle maps and scout images depicting muscle attachments employed in the biomechanical model. Left lateral (B), rostral (C) and ventral (D) views. (E) Close-up of the palatocranial region and bones of interest. Bpt, basisphenoid process; Bs, basisphenoid; Ept, epipterygoid; EptPrJ, epipterygoid–prootic joint; EptPtJ, epipterygoid–pterygoid joint; JJ, jaw joint; mAMEM, m. adductor mandibulae externus medialis; mAMEP, m. adductor mandibulae externus profundus; mAMES, m. adductor mandibulae externus superficialis; mAMP, m. adductor mandibulae posterior; mDM, m. depressor mandibulae; mLPt, m. levator pterygoideus; mPPt, m. protractor pterygoideus; mPSTp, m. pseudotemporalis profundus; mPSTs, m. pseudotemporalis superficialis; mPt, m. pterygoideus; OJ, otic joint; PBJ, palatobasal joint; Pr, prootic; Pt, pterygoid; Qu, quadrate.

Journal of Experimental Biology (2019) 222, jeb201459. doi:10.1242/jeb.201459

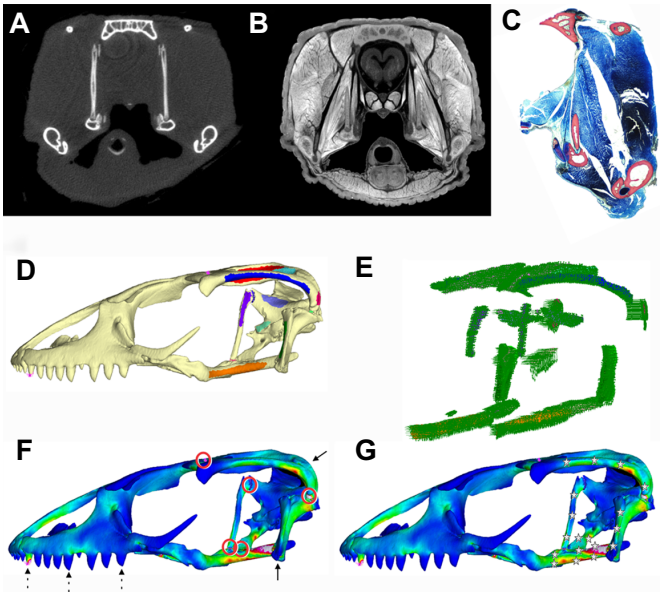

Fig. 2. Finite element analysis (FEA) workflow. (A,B) Computed tomography (CT; A) and diceCT (B) data of the specimen. (C) Histological slide of the palatobasal joint. (D) Muscle mapping in Strand7. (E) Muscle force vectors created via Boneload. (F) Locations of constraints placed on the model (arrows) and joints that were modeled (red circles). Dashed arrows represent places where constraints were placed in certain loading scenarios, while solid arrows represent constraints placed in all loading scenarios. (G) Points of interest collected on the ipsilateral side. Similar points were chosen on the contralateral side.

Unfused, flexible, kinetic joints, including the otic (quadratosquamosal) joint, frontal–parietal suture, palatobasal joint and the articulations of the epipterygoid with the pterygoid and prootic, were built using flexible linkages acting as beams (Fig. 2F) with soft tissue material properties. Four different joint linkage scenarios were created: joint-loading (JL) scenario 1: all-bone linkages; JL scenario 2: all-cartilage linkages; JL scenario 3: all-sutural ligament linkages; and JL scenario 4: mixed linkage properties based on histological results. Material properties of these linkages included bone (alligator cranial bone; Zapata et al., 2010), cartilage (Beaupré et al., 2000) and suture (McLaughlin et al., 2000). Histological data informed the construction of JL4 joint-loading model, though material properties were not derived from these data.

Muscle modeling

Jaw muscles were dissected and fascicle lengths and angular orientation data were collected to calculate physiological cross-sectional area (PCSA) of individual muscles (Fig. 2; Tables S1 and S2). Attachment sites of muscles (Fig. 1) were determined from dissection, diceCT and literature review (Fig. 3; Table S1). Muscle attachments were then mapped onto the model to determine PCSA and thus muscle loads acting upon the model (Figs 1 and 2; Tables S1 and S2). PCSA is a function of muscle volume, fiber length and muscle pennation (Gans, 1982) and can be defined by Eqn 1 (Sacks and Roy, 1982):

$$\mathrm{PCSA} = \frac{V_\mathrm{m}}{l_\mathrm{f}} \cdot \cos(\theta), \tag{1}$$

where V_m is muscle volume, l_f is fiber length and θ is the angle of pennation (Sacks and Roy, 1982). As per Sellers et al. (2017), muscle volume was treated as a frustum, or a cone with its apex cut off parallel to its base (Sellers et al., 2017). This volume can be defined by Eqn 2:

$$V_\mathrm{m} = \frac{l_\mathrm{m}}{3} \cdot \left(A_\mathrm{or} + A_\mathrm{ins} + \left(\sqrt{A_\mathrm{or} \cdot A_\mathrm{ins}}\right)\right), \tag{2}$$

where l_m is muscle length, A_or is the surface area of the muscle origin and A_ins is the surface area of the muscle insertion (Sellers et al., 2017). Origin and insertion areas were obtained from muscle attachment maps created in Strand7. Using the Boneload workflow (Grosse et al., 2007; Davis et al., 2010; Sellers et al., 2017), muscle forces were calculated from PCSAs (Table S1) using Eqn 3 (Gans, 1982):

$$F_\mathrm{m} = \mathrm{PCSA} \cdot T_\mathrm{specific}, \tag{3}$$

where F_m is muscle force and T_specific is the specific tension of muscle (Gans, 1982). We chose a value of 0.3 (Heironymus, 2006) for specific tension. The computational Matlab toolkit Boneload (Davis et al., 2010) was used to apply these forces over the area of attachment sites (Fig. 2E). Muscle resultants were then plotted as ternary diagrams to better visualize orientation and magnitude of forces (Fig. 4).

We created seven different muscle-loading scenarios where muscles were modeled as maximally active: muscle loading (ML) scenario 1: all muscles active (to establish a baseline loading); ML scenario 2: only mPPt active (to evaluate the role of mPPt); ML scenario 3: all muscles except mPPt active (to check the results of ML2); ML scenario 4: only mPt and mPPt active (to evaluate the roles of mPt and mPPt in concert); ML scenario 5: every muscle except mPt and mPPt active (to check the results of ML4); ML scenario 6: only mPPt and mLPt active (to evaluate the roles of mPPt and mLPt in concert); and ML scenario 7: no mPPt or mLPt active (to check the results of ML6). The all-muscle activation load (ML1) was applied to every linkage group (JL1–4), whereas the other six loads (ML2–7) were only applied to the histologically informed, mixed group (JL4) and the left, unilateral caudal bite group [bite point (BP) scenario 6; see below].

FEA

Constraints were placed on the model at the jaw joint, paraoccipital and supraoccipital regions to mimic constraints of cervical muscles and various bite points (Fig. 2F). Six different bite-point scenarios were tested: BP scenario 1: bilateral, rostral bite; BP scenario 2: bilateral, midpoint bite; BP scenario 3: bilateral, caudal bite; BP scenario 4: left unilateral, rostral bite; BP scenario 5: left unilateral, midpoint bite; and BP scenario 6: left unilateral, caudal bite.

To investigate stress and strain distributions within the skull, 68 points were chosen on bones of interest (Fig. 2G; Table S3), and strain components were simplified to equivalent strain (ε_eq) with Eqn 4:

$$\varepsilon_\mathrm{eq} = \frac{2}{3} \cdot \sqrt{\frac{3(e_{xx}^2 + e_{yy}^2 + e_{zz}^2)}{2} + \frac{3(\gamma_{xy}^2 + \gamma_{yz}^2 + \gamma_{zx}^2)}{4}}, \tag{4}$$

where e_{xx} is strain in the xx direction, e_{yy} is strain in the yy direction, e_{zz} is strain in the zz direction, γ_{xy} is strain in the xy direction, γ_{yz} is strain in the yz direction and γ_{zx} is strain in the zx direction. Thirty-four of these points were on the biting side of the skull, while the other 34 were symmetrical points on the balancing side. Mean stress, Von Mises strain data and principal strain were collected from the points and compared with each other. Data visualization was performed in R and Strand7 (Figs 5–9).

Journal of Experimental Biology (2019) 222, jeb201459. doi:10.1242/jeb.201459

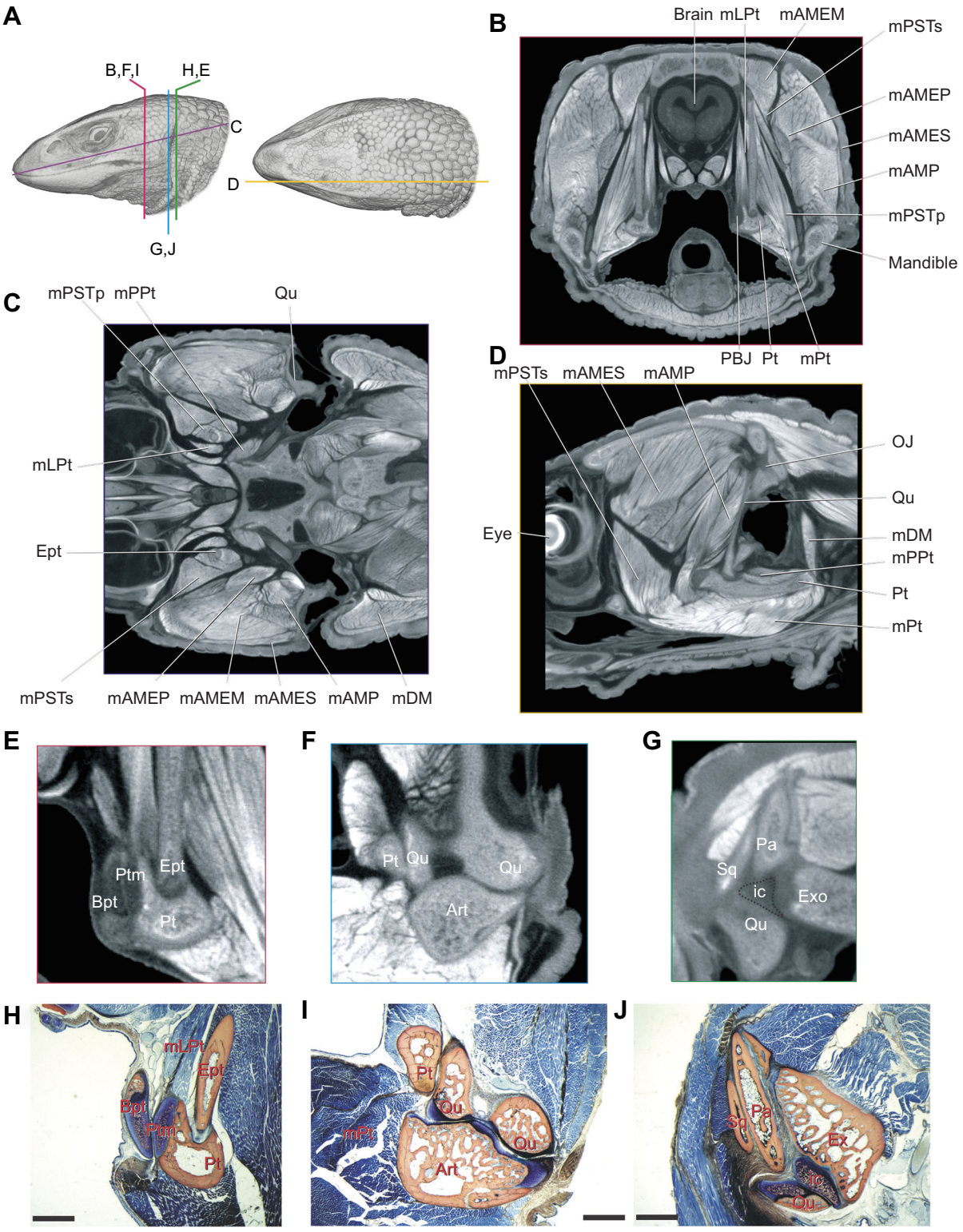

Fig. 3. See next page for legend.

RESULTS

Jaw muscles

Table S1 presents the attachments of jaw muscles used in the model. Table S2 presents the PCSA for muscles and estimated forces. Fig. 4 shows muscle resultants in ternary and 3D projection space. DiceCT (Fig. 3) and dissection revealed an arrangement of adductor and protractor musculature as described by Haas (1973), Holliday and Witmer (2008) and Holliday (2009). Briefly, m. adductor mandibulae externus superficialis (mAMES), m. adductor mandibulae externus medialis (mAMEM), m. adductor mandibulae externus profundus (mAMEP) and m. pseudotemporalis superficialis (mPSTs) provide the bulk of temporal muscles connecting the dorsal portions of the

Fig. 3. DiceCT and histology of key cranial joints in the skull of *V. exanthematicus* used to inform muscle and joint models. (A) Scout images of the head showing the location of sections B–J. (B) Rostral view of an axial slice through the palatobasal joint and adductor chamber, highlighting adductor and protractor musculature. (C) Ventral view of a horizontal section through the ventral trigeminal foramen. (D) Lateral view of a parasagittal section through the otic joint. (E) Rostral view via diceCT of an axial section through the left palatobasal joint showing articular tissues. (F) Rostral view via diceCT of an axial section through the left jaw joint showing articular tissues. (G) Caudal view via diceCT of an axial section through the left otic joint showing articular tissues. (H) Rostral view of an axial section through the left palatobasal joint showing histologically stained articular tissues. (I) Rostral view of an axial section through the left jaw joint showing histologically stained articular tissues. (J) Caudal view of an axial section through the left otic joint showing histologically stained articular tissues. Scale bars: 1 mm. Stains used for histological slides were Sanderson's Rapid Bone Stain and Van Gieson's Picrofuschsin. Art, articular; Bpt, basipterygoid process; Bs, basisphenoid; Ept, epipterygoid; EptPrJ, epipterygoid–prootic joint; EptPtJ, epipterygoid–pterygoid joint; Exo, exoccipital; ic, intercalary cartilage; mAMEM, m. adductor mandibulae externus medialis; mAMEP, m. adductor mandibulae externus profundus; mAMES, m. adductor mandibulae externus superficialis; mAMP, m. adductor mandibulae posterior; mDM, m. depressor mandibulae; mLPt, m. levator pterygoideus; mPPt, m. protractor pterygoideus; mPSTp, m. pseudotemporalis profundus; mPSTs, m. pseudotemporalis superficialis; mPt, m. pterygoideus; OJ, otic joint; Pa, parietal; PBJ, palatobasal joint; Pt, pterygoid; Ptm, pterygoid meniscus; Qu, quadrate; Sq, squamosal.

temporal region with the mandible. M. adductor mandibulae posterior (mAMP) connects the body of the quadrate to the Meckelian fossa, mPT extends from the pterygoid caudally to the caudomedial end of the mandible, and m. pseudotemporalis profundus (mPSTp) envelops the surface of the epiptyergoid to also attach to the rostromedial portion of the Meckelian fossa near the rostral edge the mPT insertion. The muscles of the orbitotemporal region, mPPt and mLPt, are quite different in orientation and size. mLPt is relatively parallel fibered, attaches across the rostral process of the prootic and extends nearly vertically to insert ventrally on a lip of bone on the medial surface of the pterygoid, dorsal to the palatobasal joint, and mPPt attaches to the basisphenoid ala temporalis and extends caudolaterally to attach to the medial surface of the pterygoid. Finally, m. depressor mandibulae (mDM) passes from the paraoccipital process to the retroarticular process. Although mDM has substantial attachments across the epaxial muscles of the neck as well, we only modeled its cranial, bony origin.

Varanus exanthematicus does not appear to have one dominant force-producing muscle, in contrast to many specialized feeders (Herrel et al., 2007; Santana and Dumont, 2011; Santana et al., 2012; Sellers et al., 2017). The jaw muscles of *V. exanthematicus* are well oriented for maintaining positional equilibrium of the palate and mandible (Fig. 4). The protractor muscles (mLPt and mPPt) are oriented askew to one another in the axial and sagittal planes, showing they have significantly different roles in mediating loads about the palatobasal and otic joints. In contrast, mLPt and mPSTp are near parallel in orientation and are antagonists across the epipterygoid–pterygoid–basipterygoid joints in the axial plane. Similarly, mAMES and mDM are both large, parallel-fibered antagonists in the sagittal plane which both elevate the jaw, albeit on

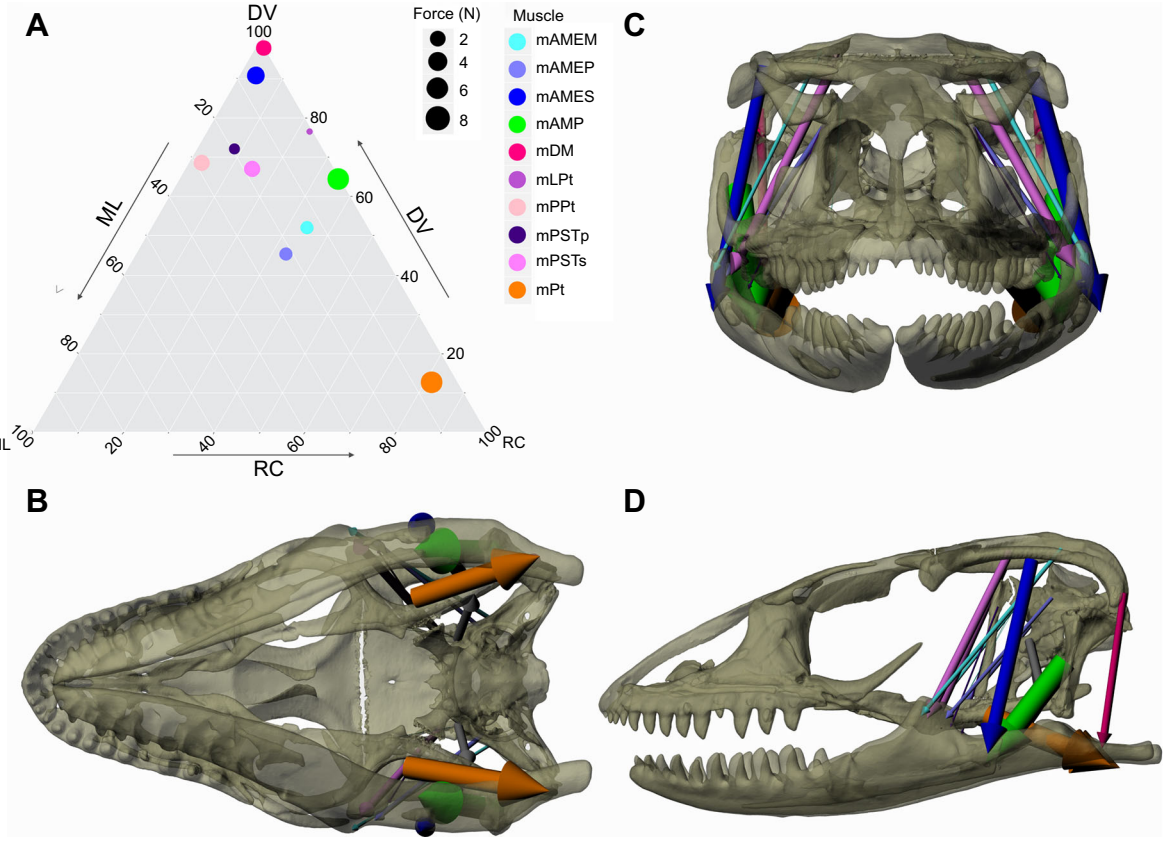

Fig. 4. Jaw muscle resultants employed in the model. (A) Ternary diagram of muscle force and orientation. (B) Ventral view of jaw muscle force resultant vectors (arrows). (C) Rostral view of jaw force muscle resultant vectors (arrows). (D) Left lateral view of jaw muscle force resultant vectors (arrows). DV, dorsoventral; mAMEM, m. adductor mandibulae externus medialis; mAMEP, m. adductor mandibulae externus profundus; mAMES, m. adductor mandibulae externus superficialis; mAMP, m. adductor mandibulae posterior; mDM, m. depressor mandibulae; ML, mediolateral; mLPt, m. levator pterygoideus; mPPt, m. protractor pterygoideus; mPSTp, m. pseudotemporalis profundus; mPSTs, m. pseudotemporalis superficialis; mPt, m. pterygoideus; RC, rostrocaudal.

Journal of Experimental Biology (2019) 222, jeb201459. doi:10.1242/jeb.201459

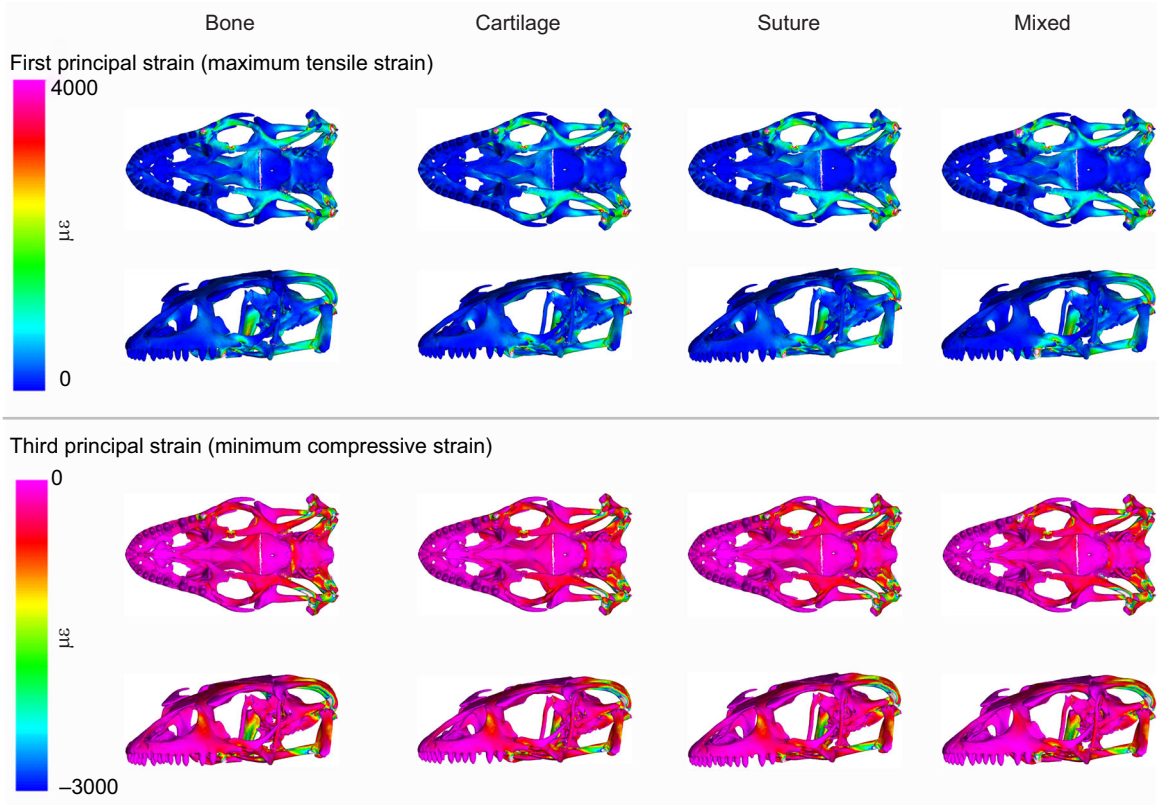

Fig. 5. Effects of joint material properties on cranial performance during symmetrical caudal bites and maximum muscle force displayed in principal strains. με, microstrain.

opposite sides of the fulcrum of the jaw joint. Finally, many of the muscles have significant mediolateral components to their orientations, predicting the torsional loading on the skull, the effects of which our model documents.

Histology

Histology of the cranial joints of *V. exanthematicus* revealed its joints are built comparably to those of geckos and other lizards (Fig. 3H–J; Payne et al., 2011). The quadrate-articular (jaw) joint is a bichondral synovial joint and the frontoparietal joint is a syndesmodial joint bridged by a sutural ligament. Sections of the palatobasal joint revealed this joint is also a bichondral synovial joint where the hyaline cartilage-capped basipterygoid process and epiphysis meet the cartilaginous vestige of the palatoquadrate cartilage, which is nestled along the medial surface of the pterygoid. The cartilage cores of the palatobasal joint are mineralized. Sections of the otic joint revealed a unichondral joint in which the hylaline cartilage-capped epiphysis of the otic process of the quadrate abuts layers of fibrous connective tissue surrounding the paraoccipital process and squamosal. This morphology is also similar to that found in the otic joint of gecko (Payne et al., 2011) and alligator (Bailleul and Holliday, 2017).

Effects of articular soft tissues

Of the four different joint treatment groups, only JL1 (all-bone joint linkage model) was significantly different from the other joint linkage treatments (Fig. 5). In JL1, strain was concentrated at joints and other narrow features of the skull. In contrast, the soft tissue linkage models (JL2–4: all-cartilage, all-suture, mixed) showed greater strain distributions in the bony elements themselves (rather than near the articulations) and were superficially comparable in loading, although there were small differences among these treatment groups. In particular, differences in articular soft tissue properties changed the polarity of loading across the palatobasal joints and basipterygoid (Figs 3, 5; Fig. S6). In the mixed linkage group (JL4) and the all-bone group (JL1), the dorsolateral portion of the balancing side basispterygoid process was tensed and the ventromedial aspect was compressed across all treatments (BP1–6, ML1–5). However, the all-cartilage group (JL2) and the all-suture group (JL3) showed compressive stresses on the dorsolateral surface of the basispterygoid process and tensile stresses on the ventromedial surface of the balancing side basispterygoid process (Figs 3, 5; Fig. S3).

Although these differences in strains were modest in magnitude, the shifting in polarity about the palatobasal joint suggest the system is not only sensitive to torsion, but also to potential changes in skeletal tissue material properties during ontogeny. The behavior of the quadrate was relatively unaffected by differences in soft tissues (Figs 3, 5; Fig. S3) but we note we did not model the pterygoquadrate joint as a suture. Due to these results, only the models built with histologically-informed, mixed linkages (JL4) will be discussed further.

Effects of muscle load

The different muscle activation scenarios resulted in a diversity of loading patterns (Figs 6–9). ML scenario 1 (ML1, full tetany of all muscles) with a left, unilateral posterior bite (BP6) resulted in asymmetric loading across the palate. Forces from the biting side were largely transmitted across the ipsilateral palatobasal joint, across the braincase and through the contralateral palatobasal joint on the balancing side. ML2 showed the protractor muscles are capable of significantly loading the palate and basispterygoid

Journal of Experimental Biology (2019) 222, jeb201459. doi:10.1242/jeb.201459

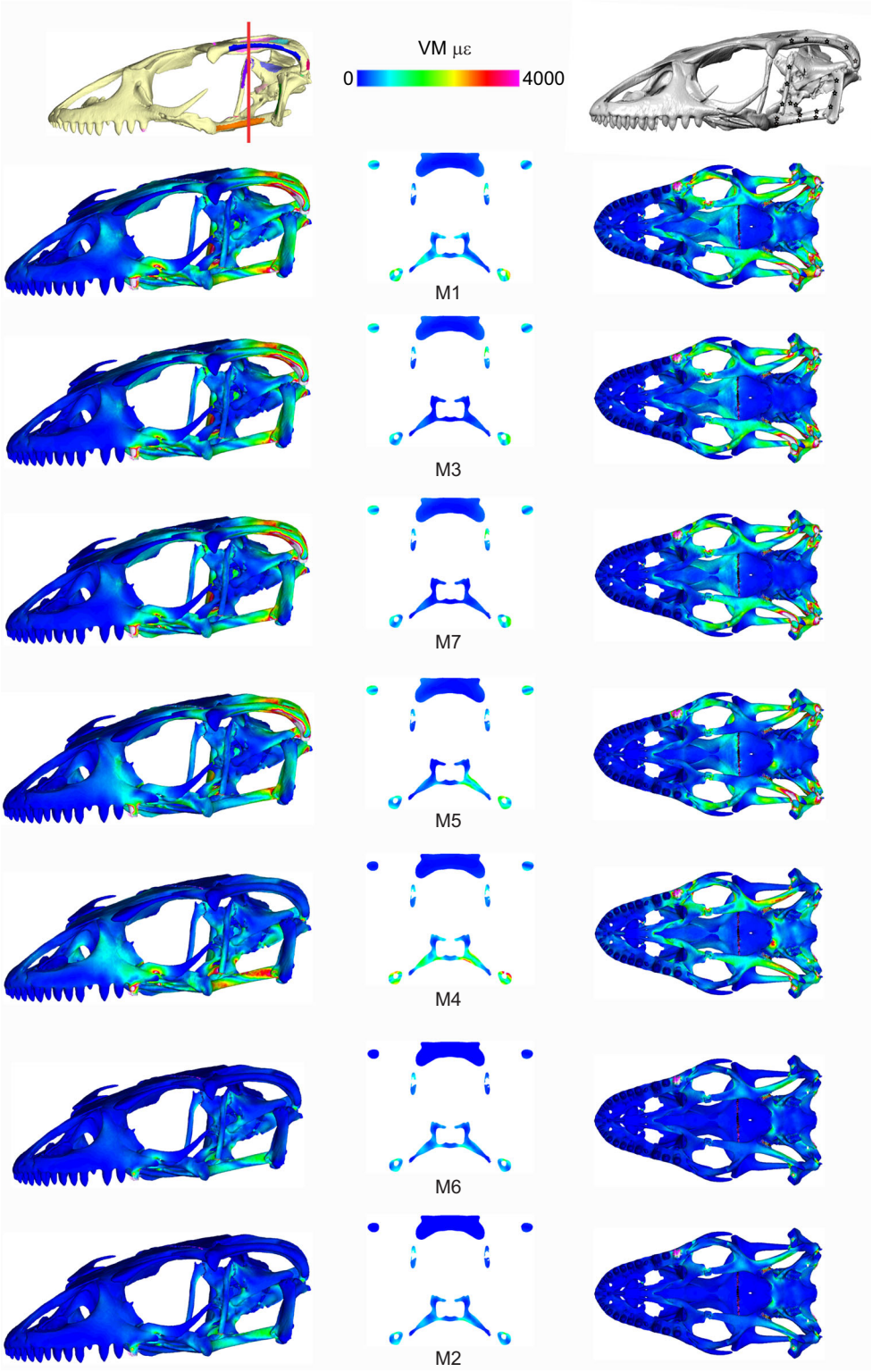

Fig. 6. Effects of muscle-loading scenarios on cranial performance of a histologically informed mixed joint model with caudal left-sided bites. Muscle loading mediates torsion and strain magnitudes in the skull of *V. exanthematicus*. Different muscle activation patterns result in significant differences in loading magnitude and polarity of working- and balancing-side temporal bars, palatocranial joints and ventral braincase. Heat maps show strains in the left, oblique lateral view, an axial section through the palatobasal joint and the left ventral view. mLPt, m. levator pterygoideus; mPPt, m. protractor pterygoideus; mPT, m. pterygoideus; VM, Von Mises. Scenarios: M1, all muscles; M2, only mPPt; M3, no mPPt; M4, only mPPt and mPt; M5, no mPPt or mPt; M6, only mPPt and mLPt; M7, no mPPt or mLPt.

process and are responsible for a large amount of loading on the basispterygoid in the all muscle activation load scenarios. In ML3, when mPPt was inactive during BP6, there was a dramatic increase in strain on the rostral midshaft and dorsal portion of the working-side quadrate (Figs 6, 7 and 9). On the working side, the midshaft and ventral portion of the rostral surface of the quadrate were weakly compressed, while the caudal surface of the quadrate and the dorsal portion of the rostral surface were tensed. On the balancing side (Figs 6, 8 and 9), similar patterns were observed; however, the ventral portion of the rostral surface was compressed. These loading polarities also exist in load cases where mPPt is active, but deactivating mPPt greatly increases the magnitude of loading. Furthermore, the working-side basispterygoid process experiences greater strains when mLPt is inactive. As expected, ML4 showed that mPPt and mPt significantly load the palate in torsion, with mPt generating most of the spiral strain pattern. This was confirmed by

Journal of Experimental Biology (2019) 222, jeb201459. doi:10.1242/jeb.201459

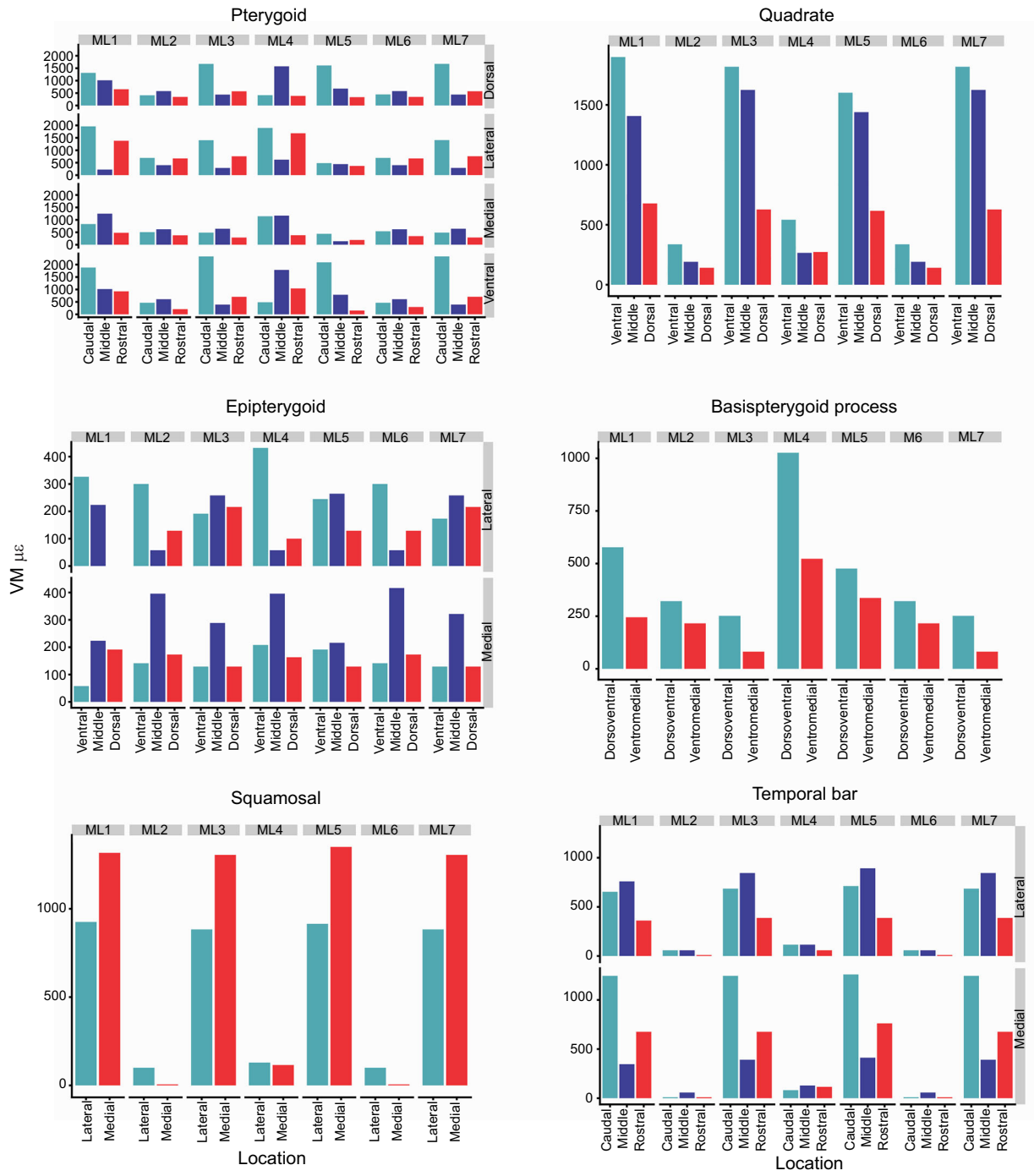

Fig. 7. Strain magnitude at points of interest on the working side of the skull modeled with mixed joints and a caudal left-sided bite under different muscle-loading conditions. The quadrate midshaft experiences more strain when mPPt and mLPt are inactive. The basispterygoid process experiences the greatest strain when mLPt is inactive, but mPPt and mPt remain active. mLPt, m. levator pterygoideus; mPPt, m. protractor pterygoideus; mPT, m. pterygoideus. Scenarios: M1, all muscles; M2, only mPPt; M3, no mPPt; M4, only mPPt and mPt; M5, no mPPt or mPt; M6, only mPPt and mLPt; M7, no mPPt or mLPt.

ML5 (no mPPt or mPt), which demonstrated that the temporal musculature weakly and indirectly loads the palate and shows minimal loading on the braincase (Figs 6–9). The balancing side of each muscle load model demonstrated similar loading patterns to the working side, albeit most structures experienced higher strain magnitudes.

Ultimately, models JL4–BP6–ML2, 3, 6 and 7 (Fig. 9) revealed that mPPt has significant biomechanical effects on the quadrate and otic joint, whereas mLPt has dramatic biomechanical effects on the basispterygoid process. Although inactivating mPPt notably lowers strain on the working-side basispterygoid process and modestly lowers strain on the balancing-side basispterygoid process, the greatest strains on the basispterygoid process are produced when mPPt and mPt are active, but mLPt is inactive (ML2,4). Furthermore, these high strains do not exist when mPPt and mLPt are inactive (but mPt remains active; ML3). Inactivation of mPPt also greatly increases strain on the caudal midshaft of the working-side quadrate regardless of mLPt activity; however, inactivation of

Journal of Experimental Biology (2019) 222, jeb201459. doi:10.1242/jeb.201459

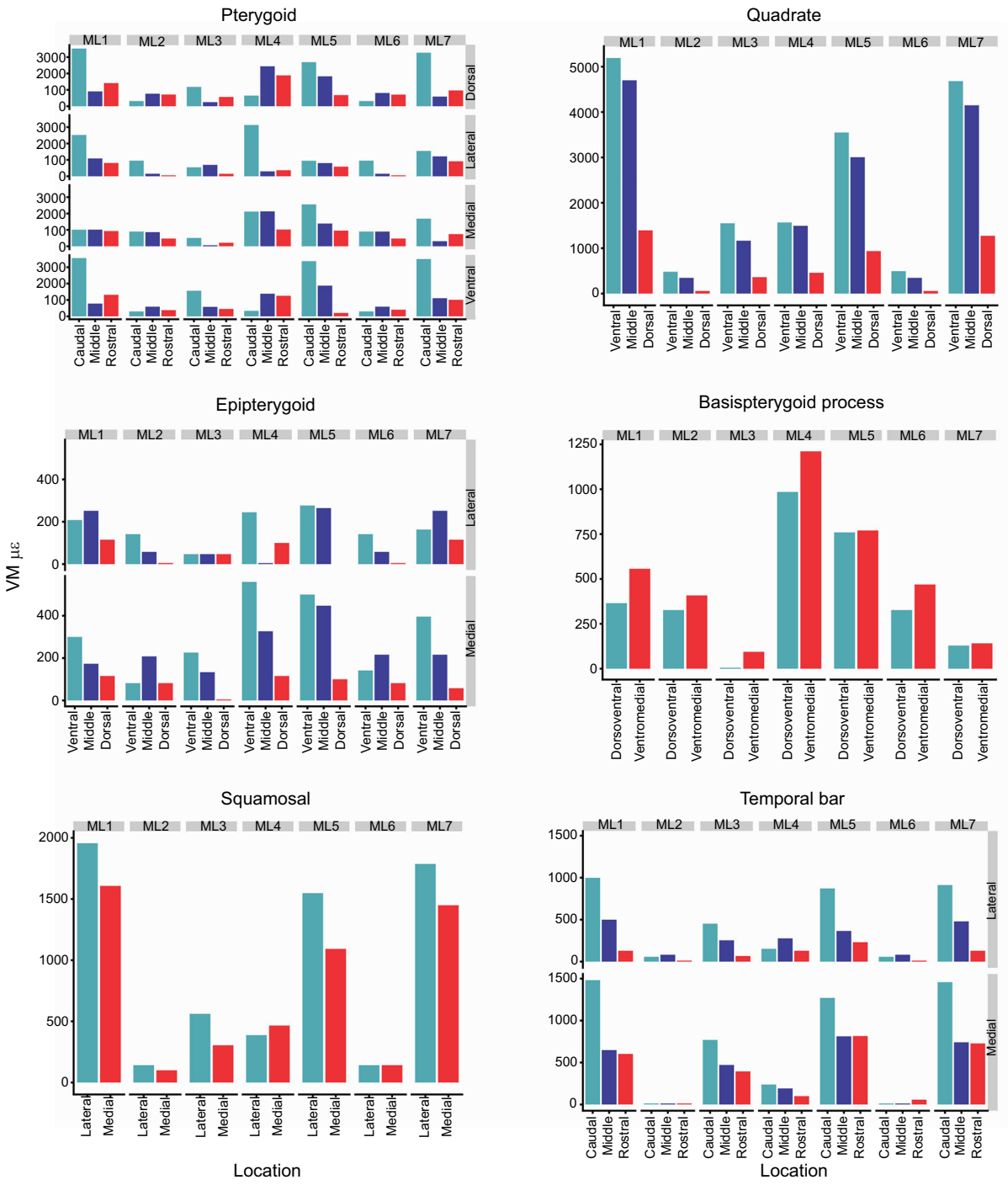

Fig. 8. Strain magnitude at points of interest on the balancing side of the skull modeled with mixed joints and a caudal left-sided bite under different muscle-loading treatments. The quadrate experiences dramatically less strain when mPPt is inactive. As for the working side, the basispterygoid process demonstrates the greatest strain when mLPt is inactive, but mPPt and mPt remain active. mLPt, m. levator pterygoideus; mPPt, m. protractor pterygoideus; mPT, m. pterygoideus. Scenarios: M1, all muscles; M2, only mPPt; M3, no mPPt; M4, only mPPt and mPt; M5, no mPPt or mPt; M6, only mPPt and mLPt; M7, no mPPt or mLPt.

mPPt dramatically reduces strain on the balancing-side quadrate. These strains modestly decrease again when mLPt and mPPt are inactive.

DISCUSSION

The savannah monitor, *V. exanthematicus*, is an ideal organism for exploring hypotheses of protractor muscle function because of its many flexible cranial joints and relatively large protractor musculature (Figs 1, 2 and 4; Table S2). Although FEA proved to be a powerful tool in elucidating the biomechanical role of this muscle, there are limitations to our model that must be recognized. Firstly, there is a dearth of resources for lepidosaur material properties (both bony and soft tissue). Second, there are no published electromyography data on mPPt activity in *Varanus*. Third, mLPt originates in part on the dura mater, which we could not accurately model for a variety of reasons; instead, we mapped the origin on the medial surface of the prootic.

Journal of Experimental Biology (2019) 222, jeb201459. doi:10.1242/jeb.201459

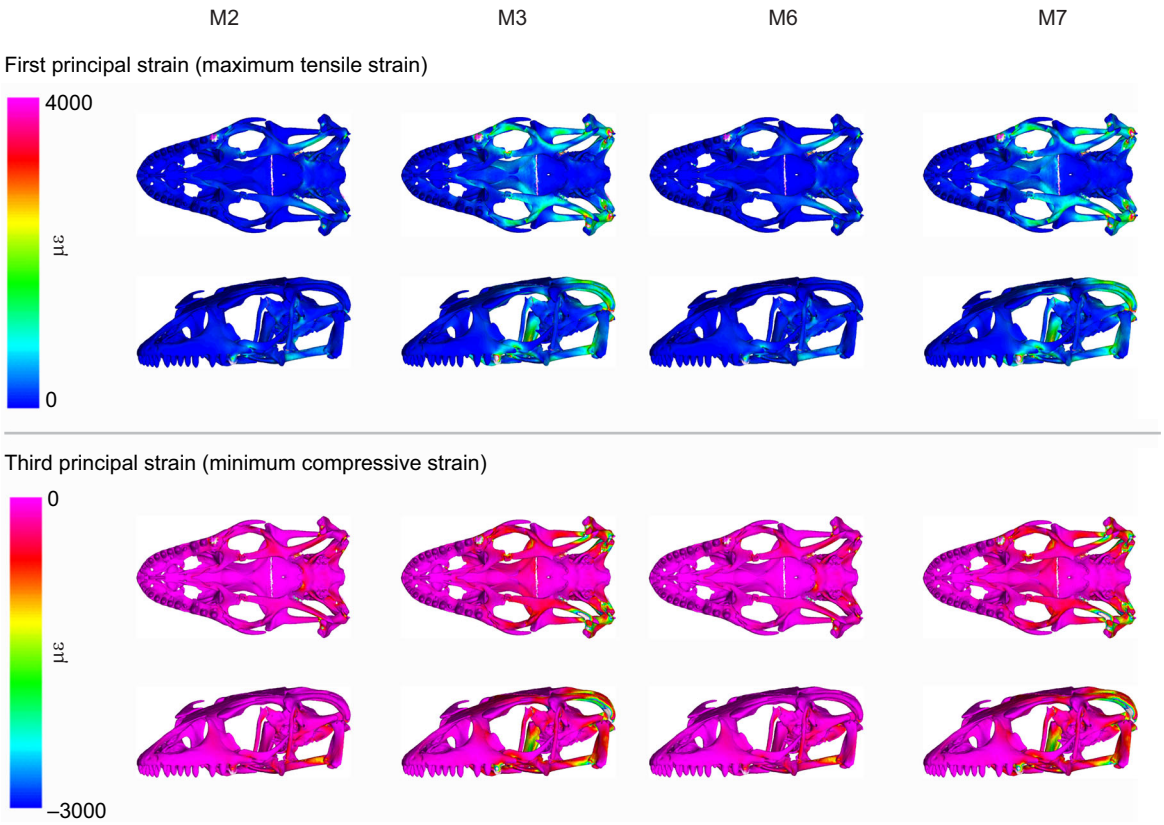

Fig. 9. Effects of muscle-loading scenarios on cranial performance of a histologically informed mixed joint model with caudal left-sided bites displayed in principal strains. mLPt, m. levator pterygoideus; mPPt, m. protractor pterygoideus; mPT, m. pterygoideus. Scenarios: M2, only mPPt; M3, no mPPt; M6, only mPPt and mLPt; M7, no mPPt or mLPt.

Finally, bony elements had to be simplified to allow meshing for FEA, and finer details of the internal architecture of elements, including much of the inner ear, were omitted.

The results of our joint-loading scenarios largely agree with previous biomechanical studies of articular soft tissues. Like sutures (Curtis et al., 2013; Ross et al., 2018), soft tissues in flexible joints alter distribution strain across the lepidosaur skull (Fig. 10). It is likely that these articular tissues reduce joint forces in other joints in a manner akin to the reduction of otic joint forces provided by streptostyly (Moazen et al., 2009). Our results also support the findings of Mezzasalma et al. (2014) that the histology of the joint may not necessarily be as important as the morphology for kinesis, as the soft tissue joint models (JL2–4) revealed similar patterns of strain and deformation. Furthermore, Bailleul et al. (2016) and Bailleul and Holliday (2017) found gross bony morphology does not always reflect the types of connective tissues in archosaur skulls. Moreover, cranial joint tissues may behave considerably differently in dynamic, rather than static loading conditions.

Our findings show that the protractor musculature (mPPt and mLPt) plays an active role in stiffening the palatobasal and otic joints and decreasing strains during feeding (Fig. 10). This supports the hypothesis that the protractor muscles play an active role in protecting the braincase and sensory capsules from detrimental loads by serving more postural roles across the otic and palatobasal joints (Holliday and Witmer, 2008). The dorsoventral and mediolateral orientations of mPPt and mLPt in *V. exanthematicus* are also well oriented antagonists to the action of mPt. When large forces from mPt abduct the palate away from the braincase, forces from mPPt and especially mLPt maintain equilibrium of the palatobasal joint and otic joint, insulting these growth plates and maintaining healthy loads in the still actively growing epiphyses (Carter et al., 1998; Carter and Beaupré, 2001). However, given the dural origin of mLPt, it remains to be seen how active the muscle is *in vivo*. Perhaps the role of the protractor musculature is to prevent extreme, pathological excursions of the palatobasal joint caused by mPt activity that could dislocate the joint. Whether this occurs as a result of cranial kinesis (e.g. the quadratic crank mechanism) or in spite of cranial kinesis remains to be clarified. Further studies are needed to examine the physiology, activation and timing of protractor muscle behavior to understand its role in cranial kinesis and palatal loading.

The loading patterns from ML1 (all-muscle activation) suggest the skull is well equipped to resist mediolateral bending and torsional forces, supporting the hypothesis of the protractor muscles protecting the cranium from feeding-generated loads (Holliday and Witmer, 2008). The pterygoids on both the working and balancing side show remarkable, torsional loading as indicated by helically shaped strain distributions (Figs 6, 9 and 10). Other elements, however, demonstrate more prominent loading from bending, such as the basispterygoid processes, temporal bars and quadrates (Figs 6–10; Fig. S4).

The tubular cross-sections of the pterygoids and upper temporal bars of the braced-frame structure of the skull suggest many bony elements may be built to resist torsional loading. This bony orientation has been shown to allow for large differences between loading in the biting and balancing sides in our study and those of other varanids (Moreno et al., 2008). One of the key elements of its load-bearing efficiency is the pterygoid, which is hollow and

Journal of Experimental Biology (2019) 222, jeb201459. doi:10.1242/jeb.201459

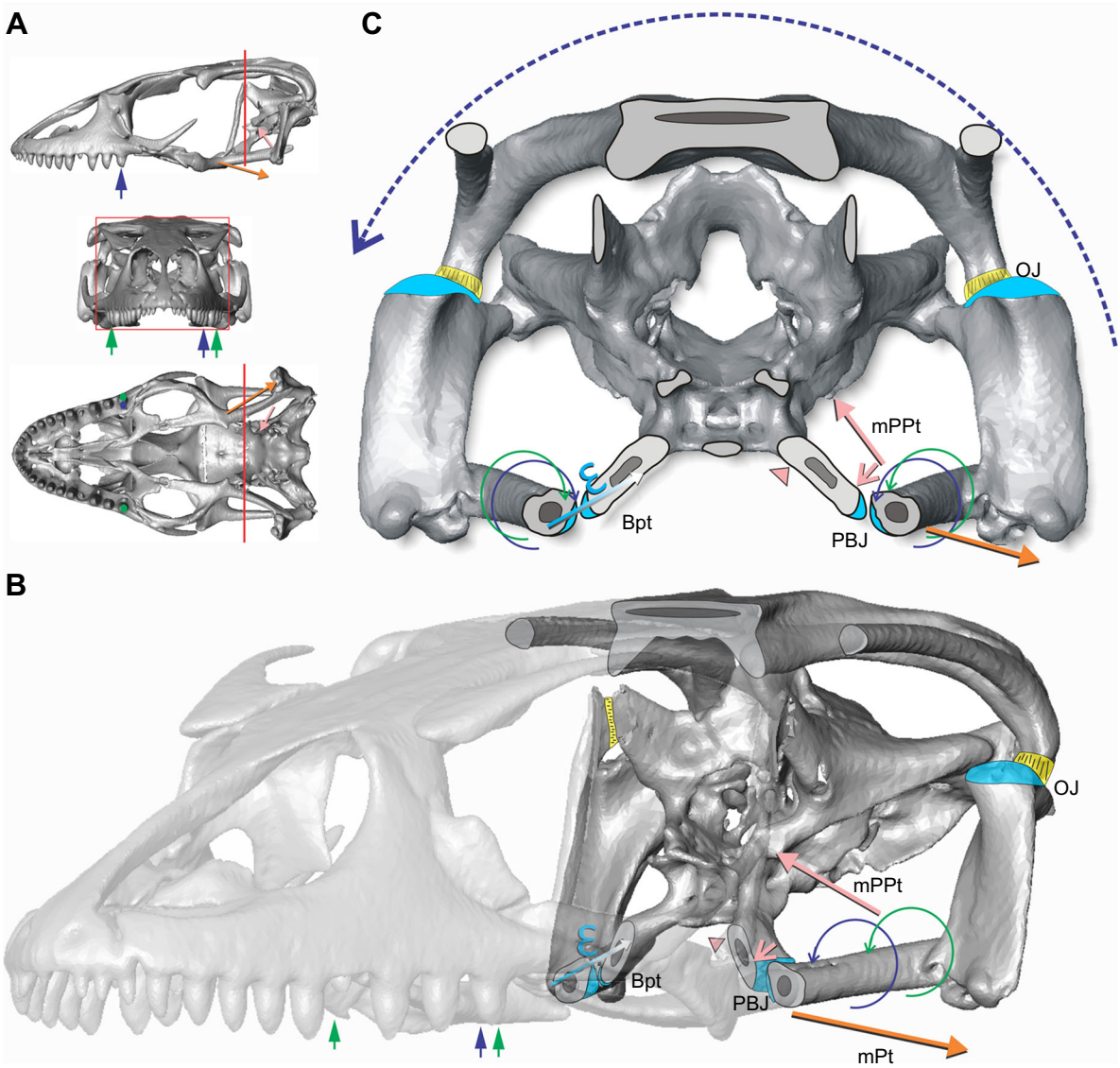

Fig. 10. Cross-sectional view of the *V. exanthematicus* palatocranial junction displaying complex interactions between articular tissues, bite points and muscle loads. (A) From top to bottom: left lateral, rostral axial and left ventral scout images displaying the location of the cross-section (red line/box), left caudal bilateral (green arrows) and unilateral (dark blue arrows) bite points, and muscle force orientations for mPPt (pink arrows) and mPt (orange arrows). (B,C) Rostral, left oblique (B) and axial (C) cross-sectional view illustrating biomechanical interactions at palatocranial junctions. Bilateral biting (green arrows) results in axial bending of the whole skull (not shown), while unilateral biting (dark blue arrows) results in counterclockwise torsion of the whole skull (dark blue dashed arrow). Bilateral biting yields positive torsion on the left pterygoid and negative torsion on the right pterygoid (green torsion arrows). Unilateral biting also yields positive torsion on the left pterygoid and negative torsion on the right pterygoid (dark blue torsion arrows). Articular tissues (light blue) cause strain (ε; light blue arrow) to be distributed away from joints and through the basispterygoid process. Forces from mPPt (long pink arrow) generate dorsoanterior bending on the basipterygoid process (pink triangle and short pink arrow). Forces from mPt pull the pterygoid laterally (orange arrow). Bpt, basispterygoid process; mPPt, m. protractor pterygoideus; mPt, m. pterygoideus; OJ, otic joint; PBJ, palatobasal joint.

tubular, indicative of resistance to bending and torsional forces (Vogel, 1988). This is supported by the helical strain pattern on the pterygoid; similar patterns have been used to support ideas of torsion-resisting elements in the mammalian masticatory apparatus (Greaves, 1985; Ross, 2001).

Kinetic competency is likely reflected by the morphology, function and behavior of the protractor musculature. Holliday and Witmer (2008) postulated that the protractor musculature is an exaptation for cranial kinesis, but is an adaptation for growth and development. Predatory feeding behaviors like unilateral biting and shaking likely result in torsional loads on the skull (Fig. S2, Movies 1 and 2) (Holliday and Witmer, 2008). Whereas crocodilians and mammals have sutured their skulls into a single rigid unit and could resist torsional loads via those mechanisms, lepidosaurs must maintain growth plates at the otic and palatobasal joints and are more vulnerable to torsional loads (Holliday and Witmer, 2008). If protractor function is an adaptation for growth and development as a response to feeding forces, there may be a relationship between protractor physiology (here defined as activation timing, orientation, fiber architecture and relative force) and the shape of an animal's palate and braincase. Are protractors necessary in a postural role when the structure of the cranium is inherently shaped to resist bending and torsion? If the braincase or palate then no longer needs the biomechanical protection of the protractor musculature, this

could free up the protractors to perform more optimized functions, such as actuating cranial kinesis (e.g. powered prokinesis). This may also explain why Cost et al. (2019) found the protractor loading on *Tyrannosaurus rex* to have little effect on loading of the palate as the animal has a relatively robust braincase and a relatively small protractor force. Comparative studies of skull shape and protractor function across reptiles are needed to address this hypothesis.

Conclusions

Through FEA, we have elucidated the role of the protractor musculature in the palatal biomechanics of *V. exanthematicus* and provided new insights into lepidosaur cranial kinesis. We found that the jaw muscles have significant mediolateral components and resultants that can impart stability across palatocranial joints. Articular tissues affect the magnitude of strains experienced across the palatobasal and otic joints. Without protractor muscle loading, the quadrate and basisphenoid process are vulnerable to higher strains, suggesting this muscle helps insulate the braincase and palatoquadrate from high loads. We found that the organization of bony elements within the skull of *V. exanthematicus* is well suited for performing under torsional loads, suggesting more focus be made on how long-axis rotation and torsion impact cranial performance in vertebrates. These findings complement and expand upon our understanding of feeding behavior, kinematics and cranial biomechanics of lizards and other reptiles. This understanding of the composition and loading environment of intracranial joints is critical to future investigations of cranial kinesis in lizards, snakes, birds and other vertebrates.

Acknowledgements

The authors thank Steve Reilly, Eric McElroy, Susan Williams and Lawrence Witmer at Ohio University, for access to specimens, equipment and Ohio University microCT scanning facilities, and Tara Selly, Jim Schiffbauer and MU X-Ray Microanalysis Core Imaging Core for scanning services at the University of Missouri. We are indebted to Betsy Dumont, Ian Grosse and participants in the 2007 Boneload summer workshop for an inspirational experience in vertebrate biomechanics. Thanks to Julian Davis for help with Boneload software. We thank Marc Jones, Callum Ross, Matt Vickaryous and Abbie Brinkhorst for discussion during the course of the project. This manuscript was greatly improved by comments from two anonymous reviewers.

Competing interests

The authors declare no competing or financial interests.

Author contributions

Conceptualization: A.T.W., C.M.H.; Methodology: A.T.W., K.M.M., K.C.S., I.N.C., C.M.H.; Software: A.T.W., K.C.S., C.M.H.; Validation: A.T.W., C.M.H.; Formal analysis: A.T.W., C.M.H.; Investigation: A.T.W., C.M.H.; Resources: C.M.H.; Data curation: A.T.W., C.M.H.; Writing - original draft: A.T.W., C.M.H.; Writing - review & editing: A.T.W., K.M.M., K.C.S., I.N.C., C.M.H.; Visualization: A.T.W., K.M.M., K.C.S., I.N.C., C.M.H.; Supervision: K.M.M., K.C.S., I.N.C., C.M.H.; Project administration: C.M.H.; Funding acquisition: K.M.M., C.M.H.

Funding

A.T.W. was funded by National Science Foundation Research Experiences for Undergraduates (NSF REU) grant IOS 1457319 and the University of Missouri Life Sciences Undergraduate Research Opportunity Program (LSUROP) and Department of Biological Sciences. This work was funded by National Science Foundation grants IOS 520100 (S. M. Reilly, A. R. Biknevicius, Ohio University), IBN 0407735 (C.M.H., L. M. Witmer) and IOS 1457319 (C.M.H., K.M.M., University of Missouri), and by the University of Missouri Department of Pathology and Anatomical Sciences.

Data availability

Data are available from the Dryad digital repository (Wilken et al., 2019): dryad.71gq288

Supplementary information

Supplementary information available online at
http://jeb.biologists.org/lookup/doi/10.1242/jeb.201459.supplemental

References

Bailleul, A. M. and Holliday, C. M. (2017). Joint histology in *Alligator mississippiensis* challenges the identification of synovial joints in fossil archosaurs and inferences of cranial kinesis. *Proc. B. R. Soc.* **284**, 20170038. doi:10.1098/rspb.2017.0038

Bailleul, A. M. and Horner, J. R. (2016). Comparative histology of some craniofacial sutures and skull-base synchondroses in non-avian dinosaurs and their extant phylogenetic bracket. *J. Anat.* **229**, 252-285. doi:10.1111/joa.12471

Beaupré, G., Stevens, S. and Carter, D. (2000). Mechanobiology in development, maintenance, and degeneration of articular cartilage. *J. Rehabil. Res. Dev.* **37**, 145-151.

Bermjeo, R., Remy, M. and Zeigler, H. P. (1992). Jaw movement kinematics and jaw muscle activity during drinking in the pigeon (*Columba livia*). *J. Comp. Physiol. A* **170**, 303-309. doi:10.1007/bf00191418

Bout, R. G. and Zweers, G. A. (2001). The role of cranial kinesis in birds. *Comp. Biochem. Physiol. A Mol. Integr. Physiol.* **131**, 1197-1205. doi:10.1016/S1095-6433(01)00470-6

Carter, D. R. and Beaupré, G. S. (2001). *Skeletal Function and Form: Mechanobiology of Skeletal Development, Aging, and Regeneration*, pp. 318. New York: Cambridge University Press.

Carter, D. R., Mikić, B. and Padian, K. (1998). Epigenetic mechanical factors in the evolution of long bone epiphyses. *Zool. J. Linn. Soc.* **123**, 163-178. doi:10.1111/j.1096-3642.1998.tb01298.x

Cost, I. N., Middleton, K. M., Echols, S. M., Witmer, L. M., Davis, J. L. Holliday, C. M. (2019). Palatal biomechanics and its significance for cranial kinesis in *Tyrannosaurus rex*. *Anat. Rec.* doi:10.1002/ar.24219

Curry, J. D. (2002). *Bones: Structure and Mechanics*. Princeton, NJ: Princeton University Press.

Curtis, N., Jones, M. E. H., Evans, S. E., O'Higgins, P. and Fagan, M. J. (2013). Cranial sutures work collectively to distribute strain throughout the reptile skull. *J. R. Soc. Interface* **10**, 20130442. doi:10.1098/rsif.2013.0442

Davis, J. L., Santana, S. E., Dumont, E. R. and Grosse, I. R. (2010). Predicting bite force in mammals: two-dimensional versus three-dimensional models. *J. Exp. Biol.* **213**, 1844-1851. doi:10.1242/jeb.041129

Evans, S. (2003). At the feet of the dinosaurs: the early history and radiation of lizards. *Biol. Rev.* **78**, 513-551. doi:10.1017/S1464793103006134

Frazzetta, T. H. (1962). A functional consideration of cranial kinesis in lizards. *J. Morph.* **111**, 287-320. doi:10.1002/jmor.1051110306

Gans, C. (1982). Fiber architecture and muscle function. *Exerc. Sports Sci. Rev.* **10**, 160-207. doi:10.1249/00003677-198201000-00006

Gignac, P. M., Kley, N. J., Clarke, J. A., Colbert, M. W., Morhardt, A. C., Cerio, D., Cost, I. N., Cox, P. G., Daza, J. D., Early, C. M. et al. (2016). Diffusable iodine-based contrast-enhanced computed tomography (diceCT): an emerging tool for rapid, high-resolution, 3-D imaging of metazoan soft tissues. *J. Anat.* **228**, 889-909. doi:10.1111/joa.12449

Greaves, W. S. (1985). The mammalian postorbital bar as a torsion-resisting helical strut. *J. Zool.* **207**, 125-136. doi:10.1111/j.1469-7998.1985.tb04918.x

Grosse, I. R., Dumont, E. R., Coletta, C. and Tolleson, A. (2007). Techniques for modeling muscle-induced forces in finite element models of skeletal structures. *Anat. Rec.* **290**, 1069-1088. doi:10.1002/ar.20568

Haas, G. (1973). Muscles of the jaws and associated structures in the Rynchocephalia and Squamata. In *Biology of the Reptilia: Morphology D*, Vol. 4 (ed. C. Gans and T. S. Parsons), pp. 285-490. New York: Academic Press.

Heironymus, T. L. (2006). Quantitative microanatomy of jaw muscle attachment in extant diapsids. *J. Morphol.* **267**, 954-967. doi:10.1002/jmor.10450

Herrel, A., De Vree, F., Delheusy, V. and Gans, C. (1999). Cranial kinesis in gekkonoid lizards. *J. Exp. Biol.* **202**, 3687-3698.

Herrel, A., Aerts, P. and De Vree, F. (2000). Cranial kinesis in geckoes: functional implications. *J. Exp. Biol.* **203**, 1415-1423.

Herrel, A., Schaerlaeken, V., Meyers, J. J., Metzger, K. A. and Ross, C. F. (2007). The evolution of cranial design and performance in squamates: consequences of skull-bone reduction on feeding behavior. *Integr. Comp. Biol.* **47**, 107-117. doi:10.1093/icb/icm014

Holliday, C. M. (2009). New insights into dinosaur jaw muscle anatomy. *Anat. Rec.* **292**, 1246-1265. doi:10.1002/ar.20982

Holliday, C. M. and Witmer, L. M. (2008). Cranial kinesis in dinosaurs: intracranial joints, protractor muscles, and their significance for cranial evolution and function in diapsids. *J. Vertbr. Paleontol.* **28**, 1073-1088. doi:10.1671/0272-4634-28.4.1073

Holliday, C. M., Ridgely, R. C., Sedlmayr, J. C. and Witmer, L. M. (2010). Cartilaginous epiphyses in extant archosaurs and their implications for reconstructing limb function in dinosaurs. *PLoS ONE* **5**, e13120. doi:10.1371/journal.pone.0013120

Holliday, C. M., Tsai, H. P., Skiljan, R. J., George, I. D. and Pathan, S. (2013). A 3D interactive model and atlas of the jaw musculature of *Alligator mississippiensis*. *PLoS ONE* **8**, e62806. doi:10.1371/journal.pone.0062806

Jones, M. E. H., Gröning, F., Dutel, H., Sharp, A., Fagan, M. J. and Evans, S. E. (2017). The biomechanical role of the chondrocranium and sutures in a lizard skull. *J. R. Soc. Interface* **14**, 20170637. doi:10.1098/rsif.2017.0637

McCurry, M. R., Mahoney, M., Clausen, P. D., Quayle, M. R., Walmsley, C. W., Jessop, T. S., Wroe, S., Richards, H. and McHenry, C. R. (2015). The relationship between cranial structure, biomechanical performance and ecological diversity in varanoid lizards. *PLoS ONE* **10**, 1-27. doi:10.1371/journal.pone.0130625

McElroy, E. J., Hickey, K. L. and Reilly, S. M. (2008). The correlated evolution of biomechanics, gait and foraging mode in lizards. *J. Exp. Biol.* **211**, 1029-1040. doi:10.1242/jeb.015503

McLaughlin, E., Zhang, Y., Pashley, D., Borke, J. and Yu, J. (2000). The load-displacement characteristics of neonatal rat cranial sutures. *Cleft Palate Craniofacial J.* **37**, 590-595. doi:10.1597/1545-1569_2000_037_0590_tldcon_2.0.co_2

Metzger, K. (2002). Cranial kinesis in Lepidosaurs: skulls in motion. In *Topics in Functional and Ecological Vertebrate Morphology*, pp. 15-46 (ed. P. Aerts, K. D'Août, A. Herrel and R. Van Damme). Shaker Publishing.

Mezzasalma, M., Maio, N. and Guarino, F. M. (2014). To move or not to move: cranial joints in european gekkotans and lacertids, an osteological and histological perspective. *Anat. Rec.* **297**, 463-472. doi:10.1002/ar.22827

Moazen, M., Curtis, N., O'Higgins, P., Evans, S. E. and Fagan, M. J. (2009). Biomechanical assessment of changes in the lepidosaurian skull. *Proc. Natl. Acad. Sci. USA* **106**, 8273-8277. doi:10.1073/pnas.0813156106

Montuelle, S. J. and Williams, S. H. (2015). *In Vivo* measurement of mesokinesis in *Gekko gecko*: the role of cranial kinesis during gape display, feeding and biting. *PLoS ONE* 10, e0134710. doi:10.1371/ journal.pone.0134710

Moreno, K., Wroe, S., Clausen, P., McHenry, C., D'Amore, D. C., Rayfield, E. J. and Cunningham, E. (2008). Cranial performance in the Komodo dragon (*Varanus, komodoensis*) as revealed by high-resolution 3-D finite element analysis. *J. Anat.* **212**, 736-746. doi:10.1111/j.1469-7580.2008.00899.x

Parr, W. C. H., Wroe, S., Chamoli, U., Richards, H. S., McCurry, M. R., Plausen, P. D. and McHenry, C. (2012). Toward integration of geometric morphometrics and computational biomechanics: new methods for 3D virtual reconstruction and quantitative analysis of Finite Element Models. *J. Theor. Biol.* **301**, 1-14. doi:10.1016/j.jtbi.2012.01.030

Payne, S. L., Holliday, C. M. and Vickaryous, M. K. (2011). An osteological and histological investigation of cranial joints in geckos. *Anat. Rec.* **294**, 399-405. doi:10.1002/ar.21329

Rayfield, E. J. (2007). Finite element analysis and understanding the biomechanics and evolution of living and fossil organisms. *Annu. Rev. Earth Planet. Sci.* **35**, 541-576. doi:10.1146/annurev.earth.35.031306.140104

Rieppel, O. (1978). Streptostyly and muscle function in lizards. *Experientia* **34**, 776-777.

Ross, C. F. (2001). *In Vivo* function of the craniofacial haft: the interorbital "Pillar". *Am. J. Phys. Anthropol.* **116**, 108-139. doi:10.1002/ajpa.1106

Ross, C. F., Porro, L. B., Herrel, A., Evans, S. E. and Fagan, M. J. (2018). Bite force and cranial bone strain in four species of lizards. *J. Exp. Biol.* **221**, jeb180240. doi:10.1242/jeb.180240

Sacks, R. D. and Roy, R. R. (1982). Architecture of the hind limb muscles of cats: functional significance. *J. Morphol.* **173**, 185-195. doi:10.1002/jmor.1051730206

Santana, S. E. and Dumont, E. R. (2011). Do roost-excavating bats have stronger skulls? *Biol. J. Linn. Soc.* **102**, 1-10. doi:10.1111/j.1095-8312.2010.01551.x

Santana, S. E., Grosse, I. R. and Dumont, E. R. (2012). Dietary hardness, loading behavior, and the evolution of skull form in bats. *Evolution* **66-8**, 2587-2598. doi:10.1111/j.1558-5646.2012.01615.x

Schwenk, K. (2000). Feeding in lepidosaurs. In *Feeding: Form, Function and Evolution in Tetrapod Vertebrates*, pp. 175-290 (ed. K. Schwenk). San Diego: Academic Press.

Sellers, K. C., Middleton, K. M., Davis, J. L. and Holliday, C. M. (2017). Ontogeny of bite force in a validated biomechanical model of the American alligator. *J. Exp. Biol.* **220**, 2036-2046. doi:10.1242/jeb.156281

Smith, K. K. and Hylander, W. L. (1985). Strain gauge measurement of mesokinetic movement in the lizard *Varanus exanthematicus*. *J. Exp. Biol.* **114**, 53-70.

Soons, J., Herrel, A., Genbrugge, A., Aerts, P., Podos, J., Adriaens, D., de Witte, Y., Jacobs, P. and Dirckx, J. (2010). Mechanical stress, fracture risk, and beak evolution in Darwin's ground finches (*Geospiza*). *Philos. Trans. R. Soc. B.* **365**, 1093-1098. doi:10.1098/rstb.2009.0280

Vogel, S. (1988). *Life's Devices: The Physical World of Animals and Plants*. Princeton, NJ: Princeton University Press.

Werneburg, I., Polachowski, K. M. and Hutchinson, M. N. (2015). Bony skull development in the Argus monitor (*Varanus panoptes*) with comments on developmental timing and adult anatomy. *Zoology* **118**, 225-280. doi:10.1016/j.zool.2015.02.004

Wilken, A. T., Middleton, K. M., Sellers, K. C., Cost, I. N. and Holliday, C. M. (2019). Data from: The roles of joint tissues and jaw muscles in palatal biomechanics of the savannah monitor (*Varanus exanthematicus*) and their significance for cranial kinesis. *Dryad Digital Repository*. https://doi.org/10.5061/dryad.71gq288

Zapata, U., Metzger, K., Wang, Q., Elsey, R. M., Ross, C. F. and Dechow, P. C. (2010). Material properties of mandibular cortical bone in the American alligator, *Alligator mississippiensis*. *Bone* **46**, 860-867. doi:10.1016/j.bone.2009.11.010

Table S1. Jaw muscle attachment sites used to estimate muscle forces.

Muscle	Origin	Insertion
mAMES	Wraps around the inferior surface of the temporal bar	Dorsal and lateral surface of the surangular
mAMEM	Caudal portion of the lateral surface of the squamosal	Lateral surface of the coronoid process
mAMEP	Dorsal surface of the basisphenoid	Caudal portion of the medial surface of the coronoid process
mAMP	Rostral surface of the quadrate	Medial surface of the surangular
mPSTs	Rostral portion of the lateral surface of the squamosal	Rostral portion of the medial surface of the coronoid process
mPSTp	Wraps around the superior portion of the shaft of the epipterygoid	Medial surface of the surangular, ventral to the coronoid process
mPt	Lateral and inferior surface of the pterygoid rostral to the palatobasal joint	Wraps around the inferior surface of the articular
mDM	Caudal surface of the squamosal	Dorsal surface of the articular
mPPt	Lateral surface of the prootic	Wraps around the superior and medial surfaces of the pterygoid caudal to the palatobasal joint
mLPt	Meninges of the brain	Dorsal midshaft crest of the pterygoid

Table S2. Measurements of jaw muscles used to calculate PCSA and muscle force to estimate muscle resultants and loads on finite element models.

Name	Muscle Length (mm)	Fasicle length (mm)	Pennation (°)	Muscle Volume (mm^3)	PCSA (mm2)	Force (N)	% Total Muscle force
L mAMES	16.51	11.00	7	304.43	1.66	4.99	7.49
R mAMES	16.57	11.05	7	226.79	1.23	3.69	5.54
L mAMEM	19.92	13.28	0	147.61	0.56	1.67	2.51
R mAMEM	20.29	13.53	0	112.68	0.41	1.23	1.85
L mAMEP	15.46	10.31	7	82.85	0.52	1.55	2.32
R mAMEP	15.59	10.39	7	100.15	0.61	1.84	2.76
L mAMP	9.17	6.11	5	154.08	2.74	8.22	12.34
R mAMP	9.69	6.46	5	171.51	2.73	8.18	12.28
L mPSTs	17.09	11.39	7	210.19	1.07	3.21	4.82
R mPSTs	17.28	11.52	7	199.44	0.99	2.98	4.47
L mPSTp	12.57	8.38	0	23.87	0.23	0.68	1.02
R mPSTp	12.49	8.32	0	23.05	0.22	0.67	1.00
L mPt	10.16	6.77	19	188.92	2.60	7.79	11.70
R mPt	11.18	7.46	19	242.55	2.75	8.25	12.39
L mDM	12.90	8.60	5	99.34	1.12	3.37	5.06
R mDM	12.95	8.63	5	103.40	1.07	3.21	4.82
L mPPt	6.31	4.21	5	29.94	0.89	2.67	4.01
R mPPt	6.02	4.01	5	25.91	0.92	2.77	4.16
L mLPt	10.95	10.95	0	5.02	0.42	0.13	0.20
R mLPt	10.93	10.93	0	6.60	0.55	0.17	0.26

Table S3. Locations of bricks of interest sampled for stress and strain on the pterygoid, epipterygoid, basipterygoid process, quadrate, squamosal and temporal bar of *Varanus exanthematicus* (Fig. 5).

Point	Abbreviation	Location
1	Rost. Vent. Pt.	Rostral end of the ventral surface of the pterygoid
2	Mid. Vent. Pt.	Midshaft of the ventral surface of the pterygoid
3	Caud. Vent. Pt.	Caudal end of the ventral surface of the pterygoid
4	Rost. Dors. Pt.	Rostral end of the dorsal surface of the pterygoid
5	Mid. Dors. Pt.	Midshaft of the dorsal surface of the pterygoid
6	Caud. Dors. Pt.	Caudal end of the dorsal surface of the pterygoid
7	Rost. Lat. Pt.	Rostral end of the lateral surface of the pterygoid
8	Mid. Lat. Pt.	Midshaft of the lateral surface of the pterygoid
9	Caud. Lat. Pt.	Caudal end of the lateral surface of the pterygoid
10	Rost. Med. Pt.	Rostral end of the medial surface of the pterygoid
11	Mid. Med. Pt.	Midshaft of the medial surface of the pterygoid
12	Caud. Med. Pt.	Caudal end of the medial surface of the pterygoid
13	Dors. Caud. Qu.	Dorsal end of the caudal surface of the quadrate
14	Mid. Caud. Qu.	Midshaft of the caudal surface of the quadrate
15	Vent. Caud. Qu.	Inferior end of the caudal surface of the quadrate
16	Dors. Rost. Qu.	Dorsal end of the rostral surface of the quadrate
17	Mid. Rost. Qu.	Midshaft of the rostral surface of the quadrate
18	Vent. Rost. Qu.	Ventral end of the rostral surface of the quadrate
19	D-L. Bpt.	Dorsolateral surface of the basispterygoid process
20	V-M. Bpt.	Ventromedial surface of the basispterygoid process
21	Rost. Lat. Temp.	Rostral end of the lateral surface of the temporal bar
22	Mid. Lat. Temp.	Midshaft of the lateral surface of the temporal bar
23	Caud. Lat. Temp.	Caudal end of the lateral surface of the temporal bar
24	Rost. Med. Temp.	Rostral end of the medial surface of the temporal bar
25	Mid. Med. Temp.	Midshaft of the medial surface of the temporal bar
26	Caud. Med. Temp.	Caudal end of the medial surface of the temporal bar
27	Dors. Lat. Ept.	Superior end of the lateral surface of the epipterygoid
28	Mid. Lat. Ept.	Midshaft of the lateral surface of the epipterygoid
29	Vent. Lat. Ept.	Ventral end of the lateral surface of the epipterygoid
30	Dors. Med. Ept.	Superior end of the medial surface of the epipterygoid
31	Mid. Med. Ept.	Midshaft of the medial surface of the epipterygoid
32	Vent. Med. Ept.	Inferior end of the medial surface of the epipterygoid
33	Lat. Sq.	Lateral surface of the squamosal
34	Med. Sq.	Medial surface of the squamosal

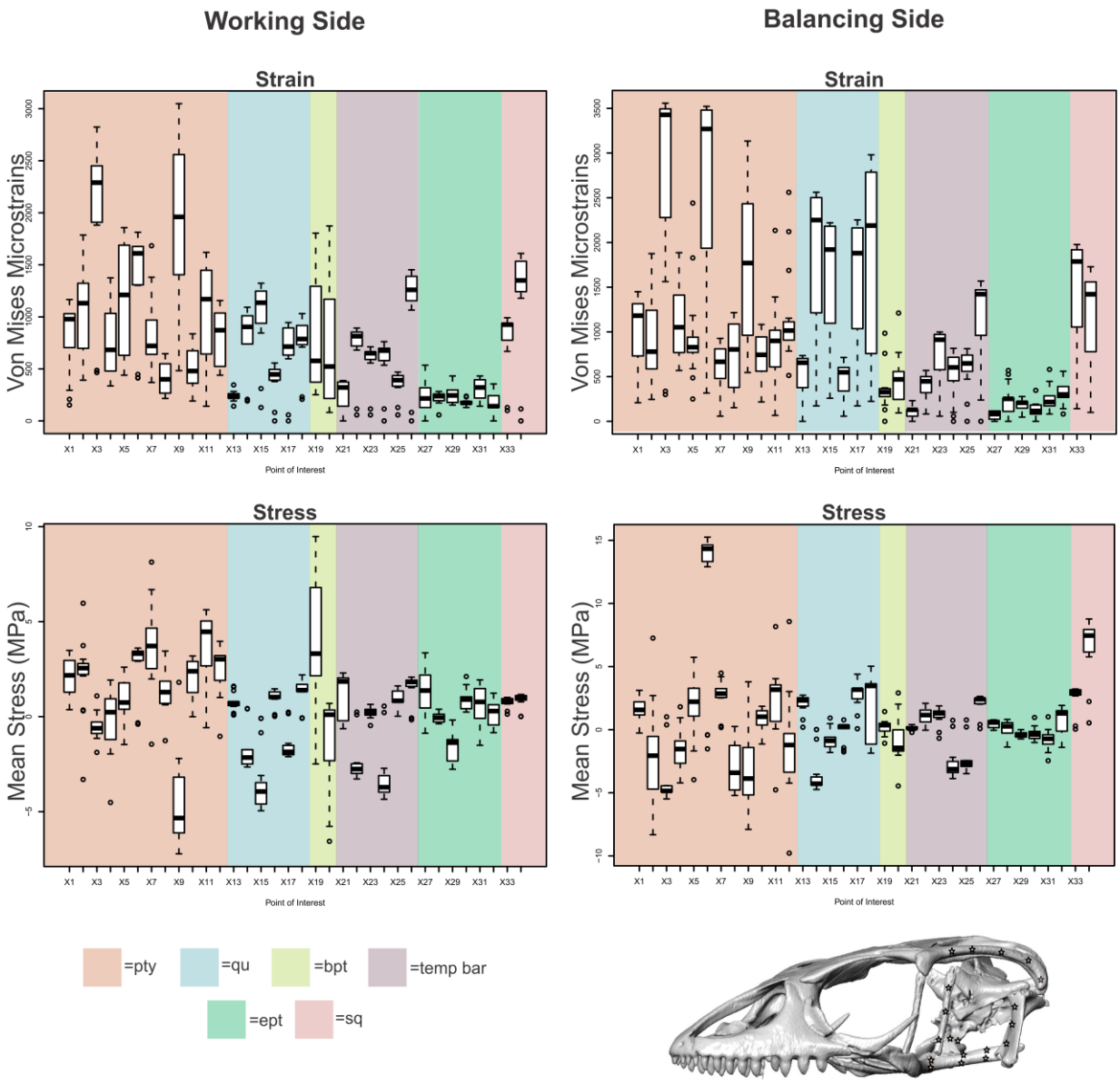

Figure S1. Summary of strains and stresses experienced by points of interest in the skull of *Varanus exanthematicus* during all modeled load cases. Not only do strain magnitudes vary considerably, but polarity and magnitude of stress shifts from tension to compression frequently depending on load case. Overall, these data illustrate a dynamically loaded system that experiences a variety of bending and torsional forces depending on feeding behavior.

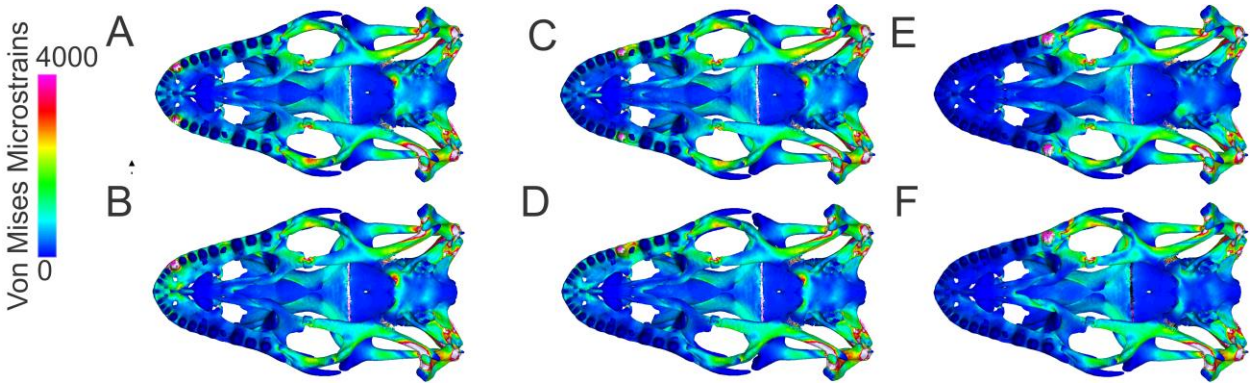

Figure S2. Effects of bite point on cranial performance of a histologically-informed mixed joint model and muscle tetany. Changing the bite point has dramatic consequences on the loading of the palate. All bite points generate torsional loading. A, bilateral rostral bite point, B, unilateral rostral bite point, C, bilateral mid bite point, D, unilateral mid bite point, E, bilateral caudal bite point, and F, unilateral caudal bite point. The six different bite point scenarios (BP1-6) yielded significant differences in cranial loading as expected with changes in bite point (Fig. 7). Anterior bite points (BP1, BP4) increase loading on the rostrum and caudal bite points (BP3 and BP6) decrease loading on the palate and braincase. In the bilateral bite models (BP1-3), loading of the rostrum, palate and braincase was relatively symmetrical on both the working and balancing sides of the skull, as opposed to the unilateral bite models (BP 4-6) which showed large differences between the working and balancing side cranial structures, one of the most striking differences being the loading of the quadrate and pterygoid. There are also noticeable differences between the basispterygoid processes of the working and balancing sides. Both the working and balancing side in every load case (BP1-6) have their respective basispterygoid processes being bent; however, the magnitude of this bending differs between the working and balancing sides. In unilateral bites, the working side dorsolateral surface of the basispterygoid

process experiences greater strain and is loaded in tension while the ventromedial surface is experiences lesser strains and is loaded in compression (Fig. 7). This contrasts with the balancing side, in which the dorsolateral surface experiences lesser strain and is still tensed, while the ventromedial surface is experiencing greater compressive loading. The position of the bite point has a large effect on the magnitude of bending occurring in both basispterygoid processes. All scenarios produced a helically-oriented loading pattern in the pterygoid bone suggesting the element experiences considerable torsion. This helical strain pattern is the same on both the balancing side and working side.

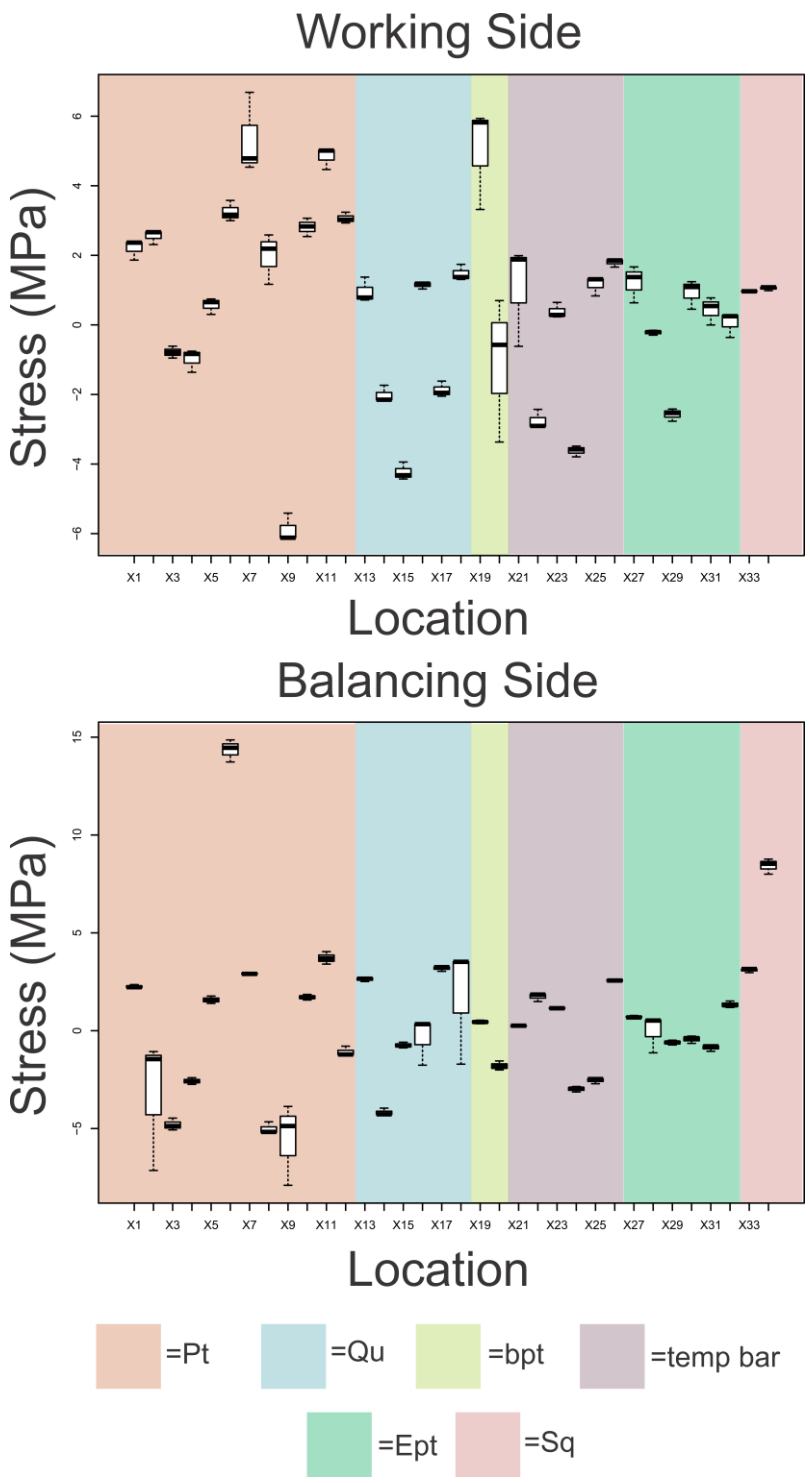

Figure S3. Summary of stress collected from points of interest in JL2-4 (all cartilage, all suture, mixed).

Movie 1. Varanus exanthematicus_Caudal Bilateral Bite_10x deformation. Rostral, axial view, left, lateral oblique view, and left, ventral view of an absolute deformation of 10 caused by bilateral caudal bite points. This bite point treatment demonstrates overall axial bending of the skull.

Movie 2. Varanus exanthematicus_Caudal Unilateral Bite_10x deformation.

Rostral, axial view, left, lateral oblique view, and left, ventral view of an absolute deformation of 10 caused by a unilateral caudal bite point. This bite point treatment demonstrates overall axial bending of the skull.